Proximity proteomics reveals a co-evolved LRRK2-regulatory network linked to centrosomes

Marita Eckert[1,4,5], Pasquale Miglionico[2,5], Francesca Izzi[1], Natalia De Oliveira Rosa[2], Marius Ueffing[3], Francesco Raimondi[2*] and Christian Johannes Gloeckner[1,3*]

[1]German Center for Neurodegenerative Diseases, 72076 Tübingen, Germany;

[2]Laboratorio di Biologia Bio@SNS Scuola Normale Superiore, 56126 Pisa, Italy;

[3]Center for Ophthalmology, Institute for Ophthalmic Research, University of Tübingen, 72076 Tübingen, Germany

[4] Graduate School of Cellular and Molecular Neuroscience, University of Tübingen, 72074 Tübingen, Germany.

[5]contributed equally to this work.

Corresponding authors:

Christian Johannes Gloeckner (johannes.gloeckner@dzne.de)

Francesco Raimondi (francesco.raimondi@sns.it)

Abstract

The Leucine-rich repeat kinase 2 (LRRK2) not only plays a vital role in familial forms of Parkinson's disease (PD) but is also considered as a risk factor for idiopathic PD. Its multi-domain architecture enables a fine-tuned regulation of its biological function by orchestrating intra- and inter-molecular interactions. Here, we present BioID proximity proteomes of LRRK2 revealing new interactors, which we further characterized by a novel evolutionary and structural bioinformatics pipeline. Co-evolutionary analysis of the protein-protein interaction network identified a structural and functional module enriched in cytoskeletal components linked to the centrosome and microtubules. Furthermore, structural modelling of binary interactions via AlphaFold-multimer revealed distinct groups of interactors engaging with LRRK2 dependent on specific conformations and epitopes. Furthermore, we identified distinct changes in the LRRK2 proximity proteome induced by the type I kinase inhibitor MLi-2 or by co-expression of the LRRK2 upstream effector RAB29. Dependent on its state of activity and conformation, these protein-protein interactions link LRRK2 to defined cellular sub-compartments, including centriolar satellites as well as vesicular sub-compartments.

Introduction

Parkinson's disease (PD) is the second most common neurodegenerative disease after Alzheimer's, it occurs mostly sporadically and is distributed with high frequency in the older generations. PD is characterized by a loss of dopaminergic neurons in the *substantia nigra* leading to the motor symptoms associated with the disease (Fahn, 2003). Several therapies targeting the symptoms, such as dopamine substitution, are practiced but so far, no causative therapy exists. About 5-10% of PD cases are inheritable (Gasser et al., 2011). *LRRK2*, localized within the PARK8 locus and coding for the Leucine-rich repeat kinase 2, is one of the genes associated with familial forms of the disease but also represents a risk factor in idiopathic PD (Paisan-Ruiz et al., 2004; Simon-Sanchez et al., 2009; Zimprich et al., 2004). The multi-domain protein LRRK2 is an active protein kinase and, at least, mutations with confirmed disease segregation, including the most common G2019S variant within its kinase domain, augment its kinase activity (Kalogeropulou et al., 2022). This makes LRRK2 an important drug target (Kluss et al., 2022b). ATP-competitive LRRK2-specific kinase inhibitors for PD-treatment are under development and in clinical trials (Jennings et al., 2022). Nevertheless, structural changes of the lung seen in non-human primates indicate a considerable small therapeutic window and additionally challenge a long-term treatment with these compounds necessary to allow a life-long reduction of augmented LRRK2 pathway activation (Miller et al., 2023). For this reason, the identification of alternative drug targets within the LRRK2-associated pathways would be a potential solution for a better control of pathophysiological alterations associated with pathogenic forms of this protein, minimizing the risk of drug-induced lung pathologies. In addition, a larger group of patients beyond LRRK2 mutation carriers might benefit from targeting more common PD-associated pathways.

Various functional studies have demonstrated a function of LRRK2 in vesicle trafficking, including presynaptic vesicles as well as autophagy and lysosomal pathways ((Piccoli et al., 2011); reviewed in: (Follett and Farrer, 2021)). In agreement with these cellular functions, LRRK2 phosphorylates a subset of Rab proteins, small G-proteins involved in vesicular transport, such as Rab8a and Rab10, which is elevated by PD-associated LRRK2 variants (Steger et al., 2017).

In common with other Roco proteins, LRRK2 features a remarkable complexity (Wauters et al., 2019). In fact, LRRK2 contains multiple scaffolding domains, not only being involved in keeping inactive LRRK2 in an auto-inhibited state, as recently demonstrated by high-resolution structures of LRRK2 (Deniston et al., 2020; Myasnikov et al., 2021), but are also involved in protein-protein interactions making LRRK2 a signaling hub possibly integrating multiple up- and down-stream signals (reviewed in: (Manzoni et al., 2015)). These studies suggest that the Roco protein LRRK2 is a tightly controlled protein kinase serving as hub and signal integrator and is most likely involved in context-specific, spatially controlled cellular responses that appear evolutionarily conserved. Quite some effort has therefore been spent on the investigation of the protein-protein interaction networks of LRRK2, mainly by using affinity-

65 based methods. Data of various studies were curated in public databases such as IntAct or STRING and
66 were also subject to meta-analysis to dissect functional LRRK2 signaling networks (Gloeckner and
67 Porras, 2020; Manzoni et al., 2015; Zhao et al., 2024; Zhao et al., 2023). However, affinity-based
68 methods face limits, given their bias for rather stable complexes which miss dynamic/ transient
69 interactions. We therefore used the BioID proximity labelling method to detect new interaction
70 partners of LRRK2. By systematically applying the BioID approach with three different BioID tags, we
71 describe the proximity proteome of LRRK2 under basal conditions. In addition, by a newly designed
72 bioinformatics workflow that estimates co-evolution of interacting partners based on their co-
73 presence in sequence genomes, we could demonstrate that the resulting BioID datasets are
74 characterized by higher co-evolution values similarly to confirmed direct interactions. Through this
75 approach, we have identified a cluster of interactors featuring a high degree of co-evolution to LRRK2
76 which is enriched in cytoskeletal proteins involved in centrosomal and ciliary dynamics. We predicted
77 the 3D complexes mediated by LRRK2 via AF-multimer, which also revealed distinct conformations and
78 interfaces associated to specific processes. Finally, to further stratify the interactome of LRRK2, we
79 looked at experimentally-defined conformational states of LRRK2, e.g. by investigating the context-
80 specific proximity proteome upon co-expression of the LRRK2 upstream effector RAB29 and upon
81 stabilization of an active-like kinase conformation by inhibition of LRRK2 with a type I ATP-competitive
82 inhibitor (Taylor et al., 2020; Wauters et al., 2019). Inhibition of LRRK2 with the type I inhibitor MLi-2
83 but not with the type II inhibitor GZD-824 lead to an enrichment of a highly specific sub interactome
84 associated with centriolar satellites.

85 **Methods**

86 ***Cloning and generation of the stable miniTurbo-LRRK2 cell line***

87 All used proximity tags have been ordered as synthetic genes (Eurofins) and subcloned via *Eco*RI and
88 *Xho*I into pcDNA3.0 (Invitrogen) allowing the expression of fusion proteins in mammalian cells under
89 the strong viral CMV promoter. Gateway Destination clones were generated by cloning a Gateway
90 cassette (Invitrogen) into an *Eco*RV site at the 3' end and in frame of the different BioID-tags [BioID
91 (Roux et al., 2012) (referred as BioID1), BioID2 (Kim et al., 2016), miniTurbo (Branon et al., 2018)]. For
92 better and comparable detection of the fusion proteins, all tags contained an N-terminal HA-tag. The
93 LRRK2 expression clones were subsequently generated by LR cloning (Invitrogen) based on ENTRY
94 clones described earlier (Guaitoli et al., 2016). The CDS of human of RAB29 has been ordered as
95 synthetic gene strand (Eurofins) with flanking attB sites to allow its direct cloning into pDONR201 by
96 BP cloning and subsequently cloned into an in-house (N)FLAG-HA Gateway destination clone by the LR
97 reaction. The HEK293 cell line (ACC-305) stably expressing miniTurbo-LRRK2 has been generated as
98 previously described (Gloeckner et al., 2007). Briefly, single colonies have been selected and tested

99 after transient transfection and selection via G418 (Sigma). The Flag-HA-CYLD vector was kindly
100 provided by Wade Harper (plasmid #22544, Addgene) (Sowa et al., 2009), the pCMV poly HA-ubiquitin
101 construct was kindly provided by D. Bohmann (Treier et al., 1994) and the pRK5-HA-Ubiquitin-K63
102 vector was kindly provided by T. Dawson (plasmind #17606, Addgene) (Lim et al., 2005).

103 ***Cell culture and proximity labelling***

104 HEK239T (ACC-635) or HEK293 stably expressing miniTurbo-LRRK2 were grown in 14 cm dishes in full
105 Dulbecco's modified medium (DMEM) supplemented with penicillin streptomycin and if not
106 mentioned otherwise with 10% FBS at 37°C in 5% CO2. The cells were grown for 8 hrs to 1 day reaching
107 a density of 50-80% until transfection with a self-made PEI reagent (Guaitoli et al., 2016). For each
108 condition, 4-6 plates have been used. If not stated otherwise, for biotinylation, cells have been
109 incubated with 50µM biotin (Sigma) in serum-free medium for up to 16 hours. In case of the mini turbo
110 tag, cells have been incubated with 50µM biotin after o/n starvation for 2h. For the determination of
111 the LRRK2-inhibitor dependent proximity proteomes, a HEK293 line stably expressing mT-LRRK2 was
112 either incubated with 1µM MLi-2, 1µM GZD-824 or DMSO (vehicle) 1h prior and during 2hrs biotin
113 incubation. For the analysis of RAB29-dependent proximity proteomes, mT-LRRK2 was either co-
114 expressed with HA-RAB29 or an empty pcDNA3.0 vector.

115 ***Affinity purification of biotinylated proteins***

116 For cell lysis, cell culture dishes were transferred to ice and culture media was removed. The cells were
117 rinsed two times with 5ml ice-cold PBS. The cells were covered with 1ml lysis buffer [0.5% Nonidet P-
118 40 Substitute (Merck), protease inhibitor cocktail (Roche), and 0.1% deoxycholic acid (Sigma-Aldrich)
119 in TBS (30mM Tris-HCl, pH7.4 and 150mM NaCl)] per 14cm dish and detached with a cell scraper. The
120 cell suspension was collected and incubated for 20-40min on an end-over-end shaker at 4°C. Lysate
121 were cleared by centrifugation (15,000xg for 10min at 4°C). The protein concentration of cleared
122 lysates was determined photometrically using a nanodrop (Thermo-Fisher Scientific) or with the BCA
123 assay (Thermo-Fisher Scientific) following the manufacturer's instructions. Biotinylated proteins were
124 purified by affinity enrichment using Strep-Tactin Superflow resin (IBA). To this end, the combined
125 lysates for each condition were incubated with an adjusted resin volume of 25µl packed beads per 14
126 cm cell culture dish. The resin was equilibrated by washing 3x with 500µl lysis buffer. The lysates were
127 incubated with the resin overnight at 4°C under constant agitation. The resin was sedimented by
128 centrifugation at 5,000xg for 3 min at 4°C, transferred to micoSpin columns (Cytiva) and subsequently
129 washed 3x in 500µl lysis buffer followed by two washes in 500µl 1x TBS to remove traces of SDS.
130 Biotinylated proteins were eluted by incubation with 400µl desthiobiotin elution buffer (2.5M, IBA).

131 The desthiobiotin eluates were precipitated by chloroform/ methanol and directly subjected to tryptic
132 proteolysis following standard protocols (Gloeckner et al., 2009) and stored at -80°C.

133 **CYLD co-expression experiment**

134 For the analysis of CYLD co-expression, cells were co-transfected with LRRK2 Y1699C, CYLD, and
135 ubiquitin (either in WT form or K63) plasmids. As negative control, CYLD plasmid was replaced by
136 pCDNA3 empty vector, to maintain the plasmid concentration constant among the different
137 conditions. For 6-wells, a total of 500ng of plasmid DNA was used for each well; for 14 cm plates, a
138 total of 8µg of plasmid DNA was used for each plate. The plasmids ratios were LRRK2:CYLD:Ubiquitin
139 1:3:1. Transfection and cell lysis were performed as described above.

140 ***SDS PAGE and Western Blots***

141 For functional evaluation of the bait proteins and to determine the biotinylation efficiency, samples
142 were subjected to SDS PAGE and analyzed by Western-blotting on PVDF membranes. To assess blotting
143 efficiency and equal loading, the membranes were stained with Ponceau S. Prior to blocking of the
144 membranes in 5% nonfat dry milk powder (BioRad) or 5% BSA (Carl Roth) in TBS with 0.1% Tween 20
145 (TBST) for 1-3h at RT, membranes were de-stained in TBST. Membranes were afterwards incubated
146 with primary antibody solutions overnight at 4°C under mild agitation. The primary antibody solution
147 was prepared for rat α-LRRK2 mAb (24D8 clone, hybridoma supernatant, generated in house (Carrion
148 et al., 2017)) 1:1000in 5% milk in TBST), rabbit α-pS935-LRRK2 mAb (Abcam, ab133450; 1:100,000 in
149 5% BSA in TBST), rabbit α-RAB10 mAb (Abcam, ab181367; 1:5,000 in 5% milk in TBST), rabbit α-pT73-
150 RAB10 mAb (Abcam, ab230261; 1:1,000 in 5% BSA in TBST), and mouse α-HA-tag (Roche, 3F10 clone,
151 Rat 1gG1; 1:1,000 in 5% milk in TBST). Membranes were washed 5x 5min in TBST prior to incubation
152 with the HRP-conjugated secondary antibodies α-rat (Jackson Immuno-Research, 112-036-062;
153 1:7,500) and α-rabbit (Jackson Immuno-Research, 111-036-045; 1:7,500), respectively. For the
154 detection of biotinylated proteins, membranes were incubated with Pierce™ High Sensitivity
155 Streptavidin-HRP (Thermo Scientific, 1:20,000 in 1% BSA in TBST) overnight at 4°C and washed the next
156 day 5x 5 min in TBST. Blots were developed with Pierce ECL Plus Western Blotting Substrate following
157 the manufacturer's protocol (Thermo Scientific) and exposed to Amersham Hyperfilm™ ECL (GE
158 Healthcare).

159 ***Mass spectrometry***

160 In solution proteolysis was performed as previously described (Gloeckner et al., 2009). Briefly,
161 chloroform/ methanol precipitates were dissolved in 50mM ammonium bicarbonate pH8.0. Cysteines
162 were reduced and alkylated by treatment with 100mM DTT and 300mM Iodoacetamide, respectively
163 following the incubation with trypsin (Sigma-Aldrich) overnight at 37°C. Samples were desalted by

164 micropipette C-18 solid-phase extraction tips (StageTip, Thermo Scientific) prior to LC-MSMS analysis.
165 Peptides were subsequently analyzed by LC-MSMS using a nanoflow HPLC system (Ultimate 3000 RSLC;
166 Thermo-Fisher Scientific) coupled to an Orbitrap Q-Exactive plus (Thermo-Fisher Scientific) tandem
167 mass spectrometer. Peptides were separated by reversed C-18 chromatography and 120-minute
168 gradients. MS1 spectra were acquired in the Orbitrap at 70K resolution. After selection of the 10 most
169 intense precursor ions from the MS1 scans for HCD fragmentation (Top 10 method), MS2 spectra were
170 acquired at 17.5K. RAW MS files were analyzed with Maxquant (version 2.0.3.1), enabling label-free-
171 quantification (LFQ with no normalization) and "match between runs" (Cox et al., 2014). For the
172 embedded Andromeda search engine, trypsin has been selected as enzyme and carbamylation was set
173 as fixed modification N-terminal acetylation was set as variable modification. The search was
174 performed against the human subset of the Uniprot/Swissprot database (release 2021_04, 20375
175 entries). The MaxQuant output was further processed by Perseus and SaintExpress.

176 ***Perseus post-processing***

177 For post-analysis, the protein groups were further processed by Perseus (v. 1.6.7). LFQ intensities of
178 the individual were assigned to the conditions and potential contaminants, reverse hits as well as IDs
179 only identified by site were filtered out. For further analysis, only IDs with a maximum number of
180 missing values of n-1 in at least one condition were considered. Remaining missing values were
181 replaced by group-wise imputation based on a normal distribution (log2 values) around the detection
182 limit (width=0.3; down shift=1.8). Intensities of the individual experiments were normalized by their
183 medians and significantly enriched proteins (condition vs control) were determined by a T-test
184 combined with an FDR filter (p=0.05, S0=0.1).

185 ***SaintExpress post-processing***

186 We followed a previously described protocol (http://proteomics.fi (Liu et al., 2020)) to select the most
187 confident interactors using the statistical framework of SAINTExpress (Teo et al., 2014), as well as a
188 reference knowledgebase for contaminants (i.e. CRAPome (Mellacheruvu et al., 2013)), to filter out
189 most likely false negative interactors. In particular, we generated the "Bait", "Prey" and "Interaction"
190 files to be subjected to the analysis pipeline from the MaxQuant "*proteinGroups.txt*" file by employing
191 the following columns: "Bait" file (IP name=EV_* or LRRK2_*, bait name=LRRK2, indicator for test and
192 negative control= C=EV_* ;T=LRRK2_*); "Interaction" file (IP name = EV_*/LRRK_*, bait name=LRRK2,
193 prey name=interaction partner gene symbol, spectral count or intensity values=LFQ intensity); "Prey"
194 file (prey (protein)name= interaction partner Uniprot accession, prey protein length=Sequence length,
195 prey gene name= gene symbol). The proteins that were not classified through the CRAPome filter,
196 were retained together with those passing the filter.

197 We unified the interactor list from the three BioID experiments. We finally retained a list of 208
198 interactors which passed the two filters. Only 45 proteins in the filtered interactor list are already
199 present in IntAct.

200 ***Graphical representation and network annotation***

201 PPI networks were analyzed by Cytoscape version 3.8.2 (Shannon et al., 2003) and were mapped to
202 available interaction from IntAct using the Cytoscape IntAct app (Ragueneau et al., 2021). Networks
203 were annotated with STRINGDB terms via the 'Stringify' function of the StringApp (Doncheva et al.,
204 2019) and functional enrichment retrieved via the same app. We annotated the networks using the
205 Auto Annotate plug-in (Kucera et al., 2016) using the Glay clustering method and calculated the labels
206 using the 'Adjacent Words' of the WordCloud algorithm considering significantly enriched GO
207 Biological processes and Cellular Compartments in which each gene of the network participated. The
208 Venn diagram shown in figure 1A has been generated with JVenn provided by the ProteoRE server
209 (Galaxy Version 2021.05.12) (Galaxy, 2024).

210 **Co-evolution based PPI stratification**

211 Co-evolution of two proteins A and B was measured as the Jaccard similarity coefficient of the set of
212 genomes containing an orthologous sequence of A and the set of genomes containing an orthologous
213 sequence of B. Orthologous sequences were collected from the Orthologous MAtrix (OMA) database
214 (Altenhoff et al., 2021) using a Python script written in-house using the PyOMADB client (Kaleb et al.,
215 2019) (Kaleb et al., 2019) (December 13, 2023, database version July 2023).

216

217 **AF-multimer prediction of binary interactions**

218 We used Alphafold-Multimer v2.3.2 (Evans et al., 2021) to generate 3D models of full-length LRRK2
219 binary interaction complexes for all the interactors shorter than 2000 residues. The databases required
220 to run AlphaFold-Multimer were downloaded on 12 January 2023 and the predictions were run with
221 the flag --max_template_date=01-01-1900, to avoid the usage of any available experimental
222 templates. Among the 5 models generated for each LRRK2 binary complex, only the best one was
223 considered for further analysis. The score used to evaluate the models was the default one used by
224 AlphaFold-Multimer (0.2*pTM + 0.8*ipTM).

225 **Interaction fingerprint**

226 AlphaFold produces probabilities for the $C_ß$-$C_ß$ distances between residues *i* and *j* to fall into a series of
227 distance bins. For each pair of residues, we calculated the expected value of such distance distribution,

228 yielding a matrix of dimension l_{LRRK2} x l_n, corresponding to the sequence lengths of LRRK2 and the *n*th
229 interacting partner, respectively Subsequently, we pooled the distogram on the interaction partner's
230 side and we assigned to each residue of LRRK2 the minimum expected distance to any residue of the
231 interactor. We refer to this vector of minimum expected distances as the interaction fingerprint of a
232 given interacting protein.

233 **RMSD calculation**

234 We compared LRRK2 conformations by performing Root Mean Square Deviation (RMSD)-based
235 clustering. To calculate the RMSD we fitted the structures using the C_α atoms of the LRRK2 chains from
236 position 983 to the end of the sequence. The N-terminal portion of the protein was excluded because
237 it's very flexible. Calculations were performed using the Superimposer function of the PDB Biopython
238 module (Cock et al., 2009) (version 1.83) through customized scripts and pipeline (Matic et al., 2023).

239 **Clustering**

240 The clustering was performed using the Ward method with the *clustermap* function from *seaborn*
241 python library (version 0.11.2). Results were displayed through matplotlib (https://matplotlib.org/)
242 and seaborn (https://seaborn.pydata.org/) libraries using customized python scripts. The number of
243 clusters chosen was one that maximized the mean Silhouette Coefficient of all samples (Rousseeuw,
244 1987) , as computed by the *silhouette_score* function in *scikit-learn* (Pedregosa et al., 2011).

245

246 **Results**

247 *Definition of cellular LRRK2 proximity proteomes with BioID1, BioID2 and miniTurbo.*

248 The elucidation of comprehensive protein-protein networks represents a powerful tool not only to
249 identify signaling pathways associated with a protein of interest but also to connect different
250 pathogenic mutations in a disease network or identify novel disease-associated proteins through
251 proximity to known proteins (Boldt et al., 2016; Kiel et al., 2011). Finally, new drug targets as well as
252 disease biomarkers might arise from this approach. For this reason, various studies addressed the
253 interatomic networks of LRRK2 in a different cellular context or model organism (Islam et al., 2016;
254 Meixner et al., 2011; Piccoli et al., 2011; Piccoli et al., 2014). However, most of the used technologies
255 rely on immuno-precipitation or pull-downs, which have a bias for considerable stable PPIs while
256 transient interactions remain underrepresented. In the last years, proximity-based methods, e.g.
257 BioID, have been developed allowing the identification of PPIs under physiological conditions and
258 within cells also covering transient interactions. The BioID approach is based on a variant of the
259 bacterial biotin ligase BirA, which has been converted to a promiscuous labeling tool by a single point

260 mutation within its active center allowing the release of the reactive intermediate biotinyl-AMP. To
261 determine the LRRK2 proximity proteome, we have generated different N-terminal fusion proteins.
262 Besides the original BioID (BioID1) tag (Roux et al., 2012), we used the BioID2 (Kim et al., 2016) as well
263 as miniTurbo, a shorter version of the TurboID tag, lacking the BirA DNA binding domain (Branon et al.,
264 2018). For reasons of comparability, all tags have been cloned in the same way, containing an N-
265 terminal HA tag for detection and a 3x(GGGS) linker between the tag and the protein of interest
266 inserted C-terminally of the tag by Gateway-cloning. All constructs were functionally assessed to
267 demonstrate biotinylation activity and to exclude that the tag interferes with the activity of LRRK2.
268 Western blot analysis shown in Supplemental Figure 1 demonstrates that all constructs allowed
269 sufficient biotinylation in cells. As expected, BioID2 and miniTurbo showed a higher labeling efficiency
270 compared to BioID1. We also confirmed that the fusion proteins are still able to phosphorylate the
271 physiological LRRK2 substrates by probing for Rab10 phosphorylated on Threonine-73. As far as their
272 transient expression is concerned, all constructs were able to phosphorylate endogenous Rab10 in
273 HEK293T cells at comparable LRRK2 expression levels (see: Supplemental Figure 1).
274 After initial functional tests, all three fusion constructs were used to determine their interactomes
275 after transient expression in HEK293T cells. To increase the stringency of the approach, a tag-only
276 control was used as reference. For the relative comparison of the LRRK2 vs. the tag-only control, the
277 expression levels were adjusted via pre-experiments and always confirmed by Western blot analysis
278 of the cell lysates. In contrast to comparing plus/minus biotin conditions, the tag-only control allows
279 to efficiently exclude natively biotinylated proteins as their degree of biotinylation is also increased by
280 the biotin treatment of the cells already by the experimental design. The data of all three proximity
281 proteomes were analyzed by SaintExpress and, alternatively, by labelfree quantification (LFQ)
282 combined with an FDR-controlled T-test as implemented in Perseus (Tyanova et al., 2016). To further
283 filter and analyze the data set, we implemented a bioinformatics pipeline based on co-evolution and
284 structural modeling by Alphafold-Multimer (Figure 1A). With BioID1, BioID2 and miniTurbo, 168, 312
285 and 241 proteins were identified, respectively, as being significantly enriched in the LRRK2-containing
286 condition over the tag-only control by the LFQ approach (Figure 1B; Supplemental Table 1).
287 SaintExpress (Teo et al., 2014) and subsequent filtering against the Crapome data of commonly found
288 false-positive hits (Mellacheruvu et al., 2013), however, appeared to be the more stringent analysis
289 compared to MS1-based label-free quantification. Based on this analysis, we created a non-redundant
290 set of 208 unique interactors, hereinafter referred to as “BioID set” which was submitted to the
291 bioinformatics post-processing pipeline.

292 *Functional-enrichment analysis of the LRRK2 proximity proteome*

293 We compared the LRRK2 BioID interactome with a reference LRRK2 interactome available from IntAct
294 (Orchard et al., 2014). We found that only 54 interactors in the filtered BioID set previously reported
295 in association with LRRK2, while the vast majority (154) were not yet reported for their interaction
296 with LRRK2 (Figure 2A,B). By integrating the LRRK2 BioID interactome with the network of known
297 interactions from Intact it is possible to define several modules of proteins interacting with each other
298 in addition to LRRK2 (Figure 2A). Among the enriched intracellular and cytosolic compartment, we
299 found terms related to microtubules (e.g. Microtubule Cytoskeleton, FDR=5.83E-15) and Centrosome
300 (FDR= 1.43E-13), emphasizing the importance of LRRK2 in microtubule organization (Figure 2C) and
301 representing the largest module of interacting proteins in the network (Figure 2A). In addition to the
302 enrichment of microtubule or cytoskeleton associated processes (e.g. FDR =6.04E-10), we also found
303 processes related to cell cycle and mitosis (e.g. "Regulation of mitotic cell cycle", FDR=9.71E-08) (Figure
304 2D).
305 Multiple protein domains instances are significantly enriched within the list of identified LRRK2
306 interaction partners (Figure 2E). In particular, we found that the Armadillo-type fold instance is the
307 most enriched one (FDR= 9.58E-06), which is found in 21 distinct interactors, followed by other
308 domains with lower, but still significant, degree of enrichment, such as "Forkhead-associated (FHA)
309 domain" (Almawi et al., 2017), found in six distinct proteins, the "DIX domain" (Ehebauer and Arias,
310 2009; Kafka et al., 2014) found in four proteins, the "K Homology domain, type 1" (Grishin, 2001) found
311 in six proteins and "Ubiquitin-like domain superfamily" (FDR<0.05), the latter being found in 11 distinct
312 interacting proteins. Interestingly, LRRK2 and its Drosophila orthologue dLRRK have been
313 demonstrated to functionally interact with the Forkhead box transcription factor FoxO1/dFoxO. In
314 particular, LRRK2-mediated phosphorylation of FoxO1 enhances its transcriptional activity leading to
315 neuronal toxicity (Kanao et al., 2010).

316 *Analysis of co-evolution reveals a cluster of proteins involved in centrosome/ microtubular dynamics*

317 We analyzed the extent of co-evolution of LRRK2 with its interactors to prioritize the most conserved
318 relationships associated to LRRK2's functions. We derived a metric for the co-evolution between two
319 interacting proteins based on the degree of co-presence, assessed through a Jaccard score, of
320 interacting gene pairs in sequenced genomes available from a reference orthology database (e.g. OMA,
321 see Methods). We found that such simple co-evolutionary metric is informative about non-enzymatic,
322 direct interactions as well as stable complexes at a human interactome-wide level (Miglionico et al.,
323 2024, in prep.; Meldal et al., 2022; Orchard et al., 2014) (Supplementary Table 2). We found similar
324 trends when focusing on LRRK2 interactions reported in IntAct, with "non-enzymatic direct" PPIs being
325 characterized by a significantly higher Jaccard score compared to those categorized as "association" or

326 “physical interaction” (Figure 3A). Intriguingly, we found that the distribution of co-evolution metrics
327 calculated for BioID interactors is significantly higher than most IntAct categories (i.e. “association”,
328 “physical”, “enzymatic direct”) and it is as high as the non-enzymatic direct interactions (Figure 3A).
329 This result suggests that interactors captured within the BioID dataset are more likely to represent
330 stable, direct interaction partners of LRRK2 with whom they co-evolved. Likewise, simple co-evolution
331 scores are predictive for LRRK2 direct interactions, particularly the non-enzymatic direct ones (Figure
332 3B; ROC AUC=0.715). In the case of the LRRK2 interactome, we found that this co-evolutionary metric
333 is more predictive of non-enzymatic direct interaction compared to another co-evolution estimate, i.e.
334 Mutual Information (ROC AUC=0.66; Supplemental Figure 2), which is instead more predictive at a
335 human proteome scale (Miglionico et al., 2024, in prep.).
336 We used the co-evolution metric to cluster LRRK2 and its interactors, which revealed groups of proteins
337 characterized by reciprocal high co-evolution (Figure 3C). The different groups of interactors are also
338 characterized by specific biological processes, which are overall mutual exclusive to each other,
339 suggesting that clusters of co-evolved proteins underpin specific functional interactions and biological
340 process (Supplemental Figure 3). Notably, the cluster containing LRRK2 (i.e. Cluster 2) is characterized
341 by on average higher co-evolution and several highly co-evolved proteins (Figure 3C). The top 10
342 proteins of Cluster 2 showing highest co-evolution are summarized in Table 1. By mapping members
343 of this cluster onto the STRING functional interaction network, using default parameters (Figure 3D,
344 see Methods), we found functional interactions for most of the members, including LRRK2. Overall,
345 STRING yielded a highly significant PPI enrichment (P-value=1.0E-16), suggesting that these proteins
346 are more likely to interact with themselves than with randomly selected proteins. Moreover, analysis
347 of the network topology revealed two distinct submodules: one entailing LRRK2 and proteins mainly
348 involved in Wnt signaling (FDR= 0.0013; Figure 3E); the second one with proteins involved in various
349 processes related to cytoskeleton (“Protein localization to microtubule cytoskeleton” FDR=2.18E-05),
350 centrosome (“Loss of Nlp from mitotic centrosomes” FDR=0.00086) and Centriole (FDR= 1.11E-05).
351 Overall, cluster 2 showed particular enrichment of compartments and cellular component terms, such
352 as “Microtubule Cytoskeleton” (FDR=3.52E-16) and “Centrosome” (FDR=7.84E-13) (Supplemental
353 Table 3). Interestingly, the single most co-evolved protein to LRRK2 is CYLD, a deubiquitinase that acts
354 as a negative regulator of dopamine neuron survival in Parkinson's disease (Pirooznia et al., 2022), but
355 that has not yet been reported in direct interaction with LRRK2. Interestingly, CYLD appears as a critical
356 bridging element between the two main submodules within Cluster 2 (Figure 3D).
357 On the other hand, cluster 1 is characterized by distinct processes, such as FAR/SIN/STRIPAK complex
358 (P-value= 0.0012) in cluster 1. Taken together, these results suggest that our co-evolution-based
359 approach was able to identify a group of LRRK2 interacting proteins, mostly associated to microtubule
360 and centrosome functions via the formation of stable, supramolecular complexes with LRRK2.

361 Likewise, co-evolution-based clustering of LRRK2 interactors from IntAct shows interactors such as
362 RAB29, RAB12, LRRK1 or SNCA among the most co-evolved partners which clustered with LRRK2
363 (Supplemental Figure 4), confirming the tight evolutionary constraint on LRRK2's functional regulation.

364 We validated the functional role of the interaction between LRRK2 and CYLD by assessing whether the
365 latter can increase the stability of the former. Interestingly, we could demonstrate that the co-
366 expression of CYLD increased the stability of Y1999C, a pathogenic variant of LRRK2 showing high levels
367 of Rab phosphorylation but impaired protein stability (Figure 3F). Given that CYLD is a K-63 selective
368 ubiquitin deubiquitinase, we co-expressed HA-tagged ubiquitin constructs, either containing a tandem
369 repeat of WT ubiquitin or a ubiquitin construct only allowing lysine 63 linkage as the other common
370 linkage lysines were preplaced by arginine (Kaleb et al., 2019). In agreement with previous
371 observations demonstrating that CYLD is a K-63 selective DUB, CYLD-mediated stabilization was also
372 greater in the presence of the K63-ubiquitin construct. The condition without CYLD co-expression
373 showed overall higher LRRK2 levels compared to the HA-WT ubiquitin condition.

374 In conclusion, our functional data indicate that the co-expression of CYLD can increase the protein
375 stability of LRRK2.

376 *AF-based modelling reveals a discrete repertoire of conformations and interfaces shaping the LRRK2*
377 *interactome*

378 We predicted 3D complexes for binary interactions of LRRK2 and 196 partners in the BioID dataset via
379 AlphaFold-multimer (AF) and characterized their interfaces and conformations (Figure 4A).
380 We structurally aligned LRRK2 conformations in the different complexes by superimposing the
381 monomeric LRRK2 chains and then calculating the pairwise distance of all the possible pairs via Root
382 Mean Squared Deviation (RMSD) (Figure 4A; Methods). We performed hierarchical clustering of LRRK2
383 structures based on RMSD, through which we identified two main clusters (Figure 4B). A smaller one
384 is characterized by conformations with lower deviation from the inactive LRRK2 structure (PDB ID:
385 7LHW), which we termed "locked" (Figure 4B-D). The main structural hallmarks characterizing the
386 "locked" conformation and inherited by the experimental inactive LRRK2 structure (PDB:7LHW)
387 (Myasnikov et al., 2021), are the LRR wrapping around the catalytic domains, particularly the kinase,
388 and a contact formed by the extended loop within the LRR repeats, which includes the hinge helix, and
389 the C-terminal WD40 (Myasnikov et al., 2021). A bigger cluster comprised conformations that are
390 characterized by a larger deviation from the inactive structure, due to a major rearrangement of the
391 LRR, ROC and COR domains, which we termed "unlocked" (Figure 4B-D). Such conformations are
392 reminiscent of the ones that we observed in the predicted LRRK2-RAB10 complex, which we validated
393 as the AF-predicted conformation best accommodating experimental XL-MS data (Guaitoli et al.,

394 2023). Intriguingly, we found that proteins interacting with LRRK2 in these two alternative
395 conformations are associated with distinct evolutionary and functional properties. Indeed, interactors
396 engaging with LRRK2 in the "locked" conformations are characterized by a significantly lower RMSD
397 (P-value=3.81E-20; Figure 4D) and higher co-evolution (P-value=1.33E-3; Figure 4E). The two groups
398 are also characterized by largely exclusively enriched processes (Figure 4F). In particular, the
399 interactors engaging with LRRK2 in the locked conformation are significantly associated to processes
400 linked to centriolar satellites (P-value=4.76E-10) and cilium assembly (P-value= 0.0001) (Figure 4G;
401 Supplemental Table 4). Those interacting with the unlocked conformations are associated with a
402 higher number of enriched processes, including cluster-specific ones such as cytoskeleton (P-value=
403 4.53E-09) or the microtubule organizing center MTOC (P-value= 6.40E-07). Hence, the predicted LRRK2
404 conformational switch might be relevant in orchestrating the interaction with partners associated with
405 distinct functions.
406 We also explored patterns of engagement of interactors with the different regions of the LRRK2 multi-
407 domain architecture. To this end, we considered the distribution of distance probabilities (i.e.
408 distograms) generated by AF for each binary interaction and mapped the most likely interacting
409 residues of the partners with respect to LRRK2 positions. We used such partner-specific "interaction
410 fingerprint" to cluster the interactome, through which we identified four clusters of proteins named
411 after the specific LRRK2 3D interfaces involved in the interaction (Figure 5A; see Methods): "Core"
412 comprises partners interacting with the LRR-ROC-COR-KIN domains (Figure 5A,B), "WD40" entails
413 complexes with the omonymous domain (Figure 5A,C), "ARM" complexes with a new site within the
414 Armadillo domain (Figure 5A,D) and "Other" complexes binding in alternative modalities or with no
415 specific binding interface (Figure 5A). The complexes predicted to link to the "Core" group have a
416 significantly higher AF confidence scores with respect to clusters of complexes engaging with either
417 WD40 domain (P-value=1.14E-8) and in "Other" modality (P-value=4.86E-14; Figure 5E). Complexes of
418 the Core group are also characterized by significantly higher RMSD from interactors of the WD40 one
419 (P-value=4.05E-3; Figure 5F), which bind LRRK2 in both locked and unlocked conformations (see
420 below). In the Core cluster we found established LRRK2 interactors, such as DVL1-2, confirming the
421 known interaction mechanism through the ROC-COR domains (Sancho et al., 2009). In the same
422 cluster, we also found novel interactors discovered within the BioID set, such as e.g. CYLD interacting
423 through the Core interface in a similar way. A second cluster displayed higher likelihood of interaction
424 with the WD40 domain (Figure 5A,C), with predicted complexes characterized by a similar interface
425 involving the binding of a short, disordered peptide stretch to a conserved crevice formed by β-
426 propeller loops of the WD40 domain (Figure 5C). WD40 domain binders might bind to LRRK2 in either
427 locked or unlocked conformation (Figure 5A, F), as also suggested by a bi-modal distribution of the
428 LRRK2 chain RMSD (Figure 5F) These interactors also displayed significantly higher co-evolution with

429 respect to “Other” LRRK2 interactors (P-value=5.57E-4; Figure 5G). The ARM cluster involves proteins
430 showing binding preferences for a new docking site on the Armadillo domain, centered around
431 residues 500-600 and mediating the interaction with proteins such as AXIN1 (Figure 5A,D). The larger
432 cluster (Other) contains proteins interacting with weaker likelihood and variable docking sites (Figure
433 5A). Among these, we also found proteins engaging with two more ARM docking sites, including one
434 (around aa 240) which has been recently shown to interact with RAB12 (Dhekne et al., 2023; Li et al.,
435 2024) and mediate a RAB29-independent LRRK2 Kinase activity activation (Purlyte et al., 2018; Zhu et
436 al., 2023), which is predicted to interact with proteins such as KIF16B. A third ARM binding region,
437 encompassing aa 354-444, corresponds to the RAB29 interaction interface found in the recently
438 determined RAB29-bound, tetrameric LRRK2 structure (Zhu et al., 2023), and is the predicted interface
439 for proteins such as NBR1 and MON2.

440 Overall, these results further support the hypothesis that interactors *de-novo* identified by proximity
441 labelling may physically interact with LRRK2 domains through specific conformations and contact
442 interfaces. Interactors lacking a strong interaction probability in the distogram might represent
443 proteins interacting with LRRK2 either transiently or indirectly.

444 *Type I but not type II inhibitors lead to conformational changes directing LRRK2 to centriolar satellites*

445 As mentioned above, LRRK2 exists in multiple conformations. Effector-mediated oligomerization to an
446 asymmetric tetramer has been demonstrated to switch LRRK2 to an active conformation (Zhu et al.,
447 2023). In addition, ATP-competitive kinase inhibitors can stabilize different conformations. While type
448 I inhibitors stabilize the kinase domain in an active-like conformation, type II inhibitors stabilize the
449 inactive conformation of the kinase domain (Deniston et al., 2020; Raig et al., 2024; Zhu et al., 2024).
450 Interestingly, type I but not type II inhibitors lead to a rapid dephosphorylation of LRRK2 phospho-sites
451 in an interdomain space downstream of the hinge-helix which locks LRRK2 in a compact inactive fold
452 by binding the C-terminal WD40 domain (Kalogeropulou et al., 2022; Myasnikov et al., 2021). We
453 therefore reasoned that specific types of inhibitors could be used to discriminate the proximity
454 proteome of the active versus inactive conformation of LRRK2. For this reason, we compared a DMSO
455 control (Figure 6B) with the highly potent LRRK2-specific type I kinase inhibitor, MLi-2 with the type II
456 inhibitor GZD-824 (Figure 6A), which was previously shown to inhibit LRRK2 in cells (Kalogeropulou et
457 al., 2022; Tasegian et al., 2021). By Western-blot, we confirmed, that LRRK2 is sufficiently inhibited at
458 a final concentration of 1µM in a HEK293 line stably expressing miniTurbo-tagged LRRK2 (Supplemental
459 Figure 5). A quantitative comparison of the different conditions based on an LFQ analysis combined
460 with an FDR-controlled T-test revealed that only upon treatment of the cells with MLi-2 but not with
461 GZD-824, we identified a set of proteins in the LRRK2 proximity proteome almost exclusively enriched
462 in proteins of the cilia assembly/ centriolar satellites (Figure 6A-E). Intriguingly, interactors determined

463 in presence of the MLi-2 inhibitor are characterized by a significantly higher co-evolution (Figure 6F)
464 compared to other BioID interactors. The complete list of significantly enriched proteins (MLi-2 vs.
465 DMSO) is shown in Table 2. Additional information is provided in Supplemental Table 1.

466 *RAB29 co-expression directs LRRK2 to well established lysosomal protein networks*

467 It has been previously shown that LRRK2 interacts with the RAB29/RAB32/RAB38 family of small G-
468 proteins and subsequently locates to post-Golgi endomembranes (Beilina et al., 2014; McGrath et al.,
469 2021; Vides et al., 2022; Waschbusch et al., 2014). Furthermore, RAB29 not only recruits LRRK2 to
470 lysosomal membranes but also induces its tetramerization (Zhu et al., 2023). For this reason, we
471 performed the BioID experiment in dependence of RAB29 co-expression to determine PPI networks
472 associated with the activated oligomeric state of LRRK2. In addition to mT-LRRK2, either RAB29 or an
473 empty vector were co-expressed. The resulting differential proximity proteome showed differentially
474 enriched proteins only for the condition where RAB29 was co-expressed, demonstrating that a small
475 portion of LRRK2 was recruited by RAB29 with lesser impact on the total proximity proteome (Figure
476 6G). This differential proteome was enriched in proteins involved in vesicular transport, including the
477 post-Golgi/ lysosomal compartment as revealed by an LFQ analysis combined with an FDR-controlled
478 T-test (Figure 6H,I). In particular, known LRRK2 effectors, namely RAB8A (Steger et al., 2017) and
479 SPAG9 (Boecker and Holzbaur, 2021; Bonet-Ponce et al., 2020; Kluss et al., 2022a) were among the
480 enriched proteins (Figure 6G,H). Furthermore, VAMP7, which is part of a SNARE complex mediating
481 autophagosome-lysosome fusion (Jian et al., 2024), was among the significantly enriched proteins
482 (Figure 6G,H). VAMP7-LRRK2 physical interaction has recently been described (Filippini et al., 2023).
483 The complete list of significantly enriched proteins is shown in Table 3. Additional information is
484 provided in Supplemental Table 1.

485 *MLi-2 and RAB29 differently modulate the shape the LRRK2 interactome*

486 We also modelled the 3D structures of the binary complexes between LRRK2 and partners from both
487 the MLi-2 and RAB29 interactomes and analyzed complex interfaces as well as LRRK2's conformations
488 (Vides et al., 2022).
489 Interface-based clustering suggests that MLi-2 interactors engage with LRRK2 through specific domain
490 regions, particularly the ones involving terminal domains (Supplemental Figure 6A), while they are
491 predicted to engage little with the catalytic domains, particularly the kinase, which is consistent with
492 the MLi-2 inhibitor function, while in the RAB29 interactome we see a more variable pattern of
493 engaged interfaces. In particular, predictions for this interactome revealed a cluster of proteins
494 interacting with LRRK2 through the ROC-COR-KIN domains, including the RAB8A substrate
495 (Supplemental Figure 6B), suggesting that in the context of RAB29 overexpression several partners

496 might bind in a substrate-like manner. Notably, this interaction modality is not observed for predicted
497 binary complexes of the MLi-2 interactome, confirming that the inhibitor prevents LRRK2 to bind
498 substrate-like partners. Moreover, we further validated the capability of the distogram-based
499 interface-fingerprint to discriminate functionally relevant LRRK2 interactors. We predicted the 3D
500 complexes of LRRK2 with known interacting Rabs, and we found out that Rab substrates clustered
501 separately from interacting RABs with distinct functions (e.g. RAB29 and RAB32; Supplemental Figure
502 7B).
503 From a LRRK2 conformational standpoint, we pooled the RAB29 and MLi-2 interactomes and clustered
504 LRRK2 conformations based on RMSD, which similarly revealed a locked and an unlocked cluster. The
505 interactors of RAB29 interactome are predicted to bind LRRK2 in both conformations, being
506 particularly enriched in the unlocked (Figure 7A). On the other hand, we found a significant enrichment
507 of MLi-2 interactors in the locked LRRK2 conformation (Fisher Exact Test P-value=0.023), further
508 suggesting that the inhibitor is predicted to favor the engagement with interaction partners which,
509 unlike substrates, do not require the interaction with the kinase domain (Figure 7A). Also, for these
510 interactors, the locked conformation has a significantly lower RMSD (P-value=3.85E-6; Figure 7D) and
511 a tendency towards higher coevolution (Figure 7E). Notably, when performing the enrichment of
512 interaction partners grouped based on conformational clustering, we could find even more cluster-
513 specific enrichment, with only one process in common between the partners in the locked and
514 unlocked conformations (Figure 7F, G; Supplementary Table 6).

515

516 **Discussion**

517 The systematic analysis of the interactomes of disease-associated proteins is a powerful tool to dissect
518 molecular networks and to identify pathways relevant for the molecular pathophysiology, for example
519 demonstrated by the comprehensive interactomic network underlying the assembly and homeostasis
520 of primary cilia (Boldt et al., 2016). Given its complex domain structure and tight regulation, LRRK2 is
521 most likely representing a scaffold protein orchestrating distinct signaling complexes, which makes the
522 analysis of its PPI networks an attractive approach to dissect context-specific signaling pathways
523 (Gloeckner and Porras, 2020). While a wealth of data is available for affinity-based identification of
524 protein-protein interactions, which have a bias for rather stable complexes, there is an unmet need
525 for the dissection of less stable and transient PPIs. The rapid development of biotin-based proximity
526 labelling technologies allowed to get information about this dark space the interactome (Qin et al.,
527 2021) and, in consequence, BioID approaches emerged to widely used methods to dissect PPI
528 networks. Most recently, proximity and affinity-based methods have even been shown to provide
529 complementary information of the interactomes (Moreira et al., 2023). We therefore systematically

530 studied the proximity interactome of LRRK2 applying three different BioID tags, BioID1, BioID2 and
531 miniTurbo. To identify direct LRRK2 interactors with high confidence form the proximity proteomes,
532 we applied a newly developed bioinformatic pipeline relaying on co-evolution*, co-expression and*
533 *protein domain architecture* to predict interaction type (Miglionico et al., 2024, in prep.). This pipeline
534 allowed the identification of a group of proteins within the proximity proteome showing a high degree
535 of co-evolution with LRRK2 which is highly enriched in proteins associated with the centrosome. This
536 is particularly interesting as pathogenic LRRK2 has previously been shown to lead to a centrosome
537 cohesion defect as well as to a shortening of primary cilia (Dhekne et al., 2018; Khan et al., 2024; Lara
538 Ordonez et al., 2022). Furthermore, defects in primary cilia emerges as a new pathophysiological
539 scheme connecting different genes involved in mendelian forms of Parkinson's disease (Mohd Rafiq et
540 al., 2024; Schmidt et al., 2022). Strikingly, in the cluster of proteins with higher co-evolution to LRRK2
541 (Cluster 2), the single protein showing the highest co-evolutionary association was the deubiquitinase
542 CYLD. The K-63 selective deubiquitinase CYLD is a key effector in the biology of primary cilia.
543 Furthermore, preliminary functional data indicate that CYLD, when co expressed, is able to increase
544 expression levels of the pathogenic variant LRRK2 Y1699C which shows a decreased protein stability.
545 In fact, this DUB has been shown to control apical docking of basal bodies in ciliated epithelial cells
546 (Eguether et al., 2014). It also regulates centrosomal satellites proteostasis by counteracting the E3
547 ubiquitin ligase MIB1 (Douanne et al., 2019). Furthermore, CYLD has been shown to deubiquitinate
548 Cep70 and to inactivate HDAC6 thereby mediating ciliogenesis (Yang et al., 2014). Interestingly, a
549 missense mutation has recently been shown to be a causative gene for FTD-ALS (Dobson-Stone et al.,
550 2020). Most importantly, as the deubiquitinase CYLD is part of the PINK1/parkin pathway to regulate
551 cellular levels of PARIS (ZNF746), it is a critical regulator of mitochondrial biogenesis thereby acting as
552 a negative regulator of dopamine neuron survival in Parkinson's disease. In fact, CYLD inhibition has
553 been shown to ameliorate mitochondrial pathologies in cellular PD models which makes CYLD a
554 promising target for therapeutic intervention for PD and other neurodegenerative diseases (Pirooznia
555 et al., 2022). The E3 ligase parkin preserves mitochondrial homeostasis via the PARIS/PGC-1a axis
556 (Stevens et al., 2015; Zheng et al., 2017). Noteworthy, the PD risk variant LRRK2 G2385R has recently
557 been shown to alter mitochondrial biogenesis via the PGC-1a pathway, leading to reduced PGC-1a
558 levels similarly to a PARKIN knock-out in DA neurons (Kumar et al., 2020; Xue et al., 2023). PARKIN-
559 deficient DA neurons show increased PARIS and decreased PGC-1a levels (Kumar et al., 2020). In
560 conclusion, this indicates that LRRK2/CYLD signaling at one hand and Parkin signaling at the other hand
561 might converge at the level of PARIS.

562 The second most co-evolved interactor found in Cluster 2 was the cilia-associated protein CEP85, which
563 plays a role in centrosome disjunction (Chen et al., 2019). This is of particular interest as pathogenic
564 LRRK2 variants lead to a centrosomal cohesion phenotype in patient-derived cells (Lara Ordonez et al.,

565 2019). Notably, the cohesion phenotype is also seen in EBV-transformed lymphoblastoid cell lines from
566 iPD patients which can be reverted by LRRK2 kinase inhibition (Naaldijk et al., 2024). Importantly,
567 Cluster 2 also contains the autophagy cargo protein p62/sequestosome-1. This protein has previously
568 been identified as LRRK2 interactor and substrate (Kalogeropulou et al., 2018; Park et al., 2016).
569 SQSTM1 is also linked to PD pathophysiology via the Pink1/Parkin pathway (Shin et al., 2020). In
570 addition, Cluster 2 points towards other pathways which have been previously linked to PD pathology.
571 In particular, SNAP47 is part of the STX17-SNAP47-VAMP7/8 pathway, which has been shown to be
572 involved in selective autophagy – a process not only essential for the homeostasis of primary cilia but
573 also for mitophagy (Jian et al., 2024). Phospho-ubiquitin chains generated by PINK1/Parkin activity can
574 recruit autophagy adaptors including the ubiquitin adaptor SQSTM1/p62 linking the PINK1/Parkin-
575 dependent pathway to mitophagy (Geisler et al., 2010). All three proteins participate in the
576 recruitment of the autophagy machinery to aged or dysfunctional mitochondria, which are eventually
577 enclosed inside an autophagosome and subjected to the lysosome for degradation (Wilhelm et al.,
578 2022).

579 Interestingly, also the kinesin motor protein and PX-domain containing protein KIF16B was among the
580 top hits which is involved in vesicle trafficking and receptor recycling. It binds to PdIns(3)P by its unique
581 PX domain and promotes the circulating cargo movement from early endosomes to the plasma
582 membrane (Li et al., 2020). Interestingly, it has been found to be associated with lipid droplets
583 (Bersuker et al., 2018). In turn, increased RAB8a phosphorylation by pathogenic LRRK2 variants, has
584 been shown to promote lipid storage (Yu et al., 2018), indicating that the functional interaction of
585 LRRK2 and KIF16B might contribute to alterations in the neuronal lipid homeostasis associated with PD
586 pathology (Hallett et al., 2019).

587 Furthermore, induced by conformational changes upon MLi-2 inhibition, associated with a rapid and
588 almost complete dephosphorylation of LRRK2 in a disordered domain downstream of the hinge helix,
589 we identified a molecular network around PCM1, OFD1 and CEP131 strongly suggesting a link between
590 LRRK2 and centriolar satellites. Strikingly, the proteins interacting with LRRK2 in presence of MLi-2
591 displayed the highest degree of co-evolution, suggesting that the connection between LRRK2 and
592 centriolar satellites is highly conserved. The conformational changes induced by binding of type I
593 inhibitors might result in a phase transition of LRRK2 into centriolar satellites preventing 14-3-3 binding
594 and thereby shifting the equilibrium towards the dephosphorylated protein. A similar mechanism has
595 been shown for CEP131, which is extracted from centriolar satellites by phosphorylation and
596 subsequent binding of 14-3-3 (Tollenaere et al., 2015). Centriolar satellites not only play an essential
597 role in the biogenesis of primary cilia (Hall et al., 2023) but also play a role in the degradation of
598 proteins by driving the assembly of aggresomes (Prosser et al., 2022). In fact, also LRRK2 has been

599 shown to interfere with aggresome formation preceding autophagic clearance (Bang et al., 2016).
600 Nevertheless, one caveat might be seen in the fact that LRRK2 inhibition with type I inhibitors induces
601 its destabilization and degradation.

602 Structural prediction of LRRK2 binary complexes with AF revealed distinct interfaces within each
603 determined interactome. While several interactors preferentially engage with the catalytic core of the
604 protein, including the ROC and KIN domains, others are more likely to interact on terminal domains
605 (e.g. ARM or WD40). We predicted the interaction on the kinase domain for several interactors of the
606 BioID interactome as well as the one obtained in the presence of RAB29 over-expression, including the
607 known substrate RAB8A. The engagement in a substrate-like fashion with the catalytic core entails the
608 opening of the LRRK2 structure, with the detachment of the LRR and rearrangement of the entire N-
609 term domains. We previously shown that this conformation, that we similarly predicted for the LRRK2:
610 RAB10 complex, is compatible with distance restraint obtained by mass spectrometric mapping of
611 chemical crosslinking sites via XL-MS (Guaitoli et al., 2023). Moreover, if superimposed on the active-
612 like conformation of the most recent LRRK2 tetrameric structure, such predicted complexes fit very
613 well on the rest of the oligomer, with no clashes between the modelled LRRK2 chain and the rest of
614 the tetramer, further supporting the plausibility of such complexes (Guaitoli et al., 2023). We speculate
615 that partners engaging in a such a way might represent putative substrate or might regulate the kinase
616 domain function. Strikingly, we rarely observed such interaction interface for interactors enriched in
617 presence of the MLi-2 inhibitor, which bind more frequently to the locked conformation of LRRK2.

618 In conclusion, combining proximity proteomics with co-evolutionary and structural information helped
619 identifying distinct molecular networks linking LRRK2 to centrosomal biology and primary cilia. The
620 data may foster future functional analysis to father dissect these pathways to get a detailed picture of
621 the molecular pathophysiology underlying the cilia phenotypes caused by genetic variants in different
622 genes underlying familial forms of Parkinson's disease.

623

624 **Data availability**

625 The mass spectrometry proteomics data have been deposited to the ProteomeXchange Consortium
626 via the PRIDE (Perez-Riverol et al., 2022) partner repository with the dataset identifier PXD048832 and
627 10.6019/PXD048832 (BioID1, BioID2, miniTurbo), PXD048806 and 10.6019/PXD048806 (LRRK2
628 proximity-proteomes MLi-2 vs. GZD-824) as well as PXD048808 and 10.6019/PXD048808 (RAB29 co-
629 expression). The data will be released with the final publication of the peer-reviewed manuscript. The
630 BioID interaction network and associated co-evolutionary and structural analysis can accessed at the

631 following URL: (https://dip.bioinfolab.sns.it/explore/). All data presented in the preprint version of the
632 manuscript, including MS RAW files, can be obtained upon request.

633 **Author contributions**

634 M.E. and F.I. performed BioID experiments. M.E., F.I., P.M., F.R. and C.J.G. analyzed the primary BioID
635 data. P.M. and F.R. performed the post-analysis of primary BioID data. P.M., N.D.R. and F.R. wrote the
636 code for the bioinformatic workflow. C.J.G., F.R. and M.U. designed the study. M.E., F.I., P.M., F.R. and
637 C.J.G. wrote the manuscript.

638 **Acknowledgements**

639 We are grateful to the staff of the Core Facility for Medical Proteomics at the medical faculty of the
640 University of Tübingen for technical assistance. Furthermore, we gratefully acknowledge
641 computational resources of the Center for High Performance Computing (CHPC) at SNS. CJG received
642 funds from The Michael J. Fox Foundation for Parkinson's Research (grant ID: MJFF-8068.02, MJFF-
643 8068.04 and MJFF-023920) and iMed – the Helmholtz Initiative on Personalized Medicine.

644 **Literature**

645 Almawi, A.W., Matthews, L.A., and Guarne, A. (2017). FHA domains: Phosphopeptide binding and
646 beyond. *Prog Biophys Mol Biol 127*, 105-110 doi: 10.1016/j.pbiomolbio.2016.12.003.
647 Altenhoff, A.M., Train, C.M., Gilbert, K.J., Mediratta, I., Mendes de Farias, T., Moi, D., Nevers, Y.,
648 Radoykova, H.S., Rossier, V., Warwick Vesztrocy, A., Glover, N.M., and Dessimoz, C. (2021). OMA
649 orthology in 2021: website overhaul, conserved isoforms, ancestral gene order and more. *Nucleic*
650 *acids research 49*, D373-D379 doi: 10.1093/nar/gkaa1007.
651 Bang, Y., Kim, K.S., Seol, W., and Choi, H.J. (2016). LRRK2 interferes with aggresome formation for
652 autophagic clearance. *Mol Cell Neurosci 75*, 71-80 doi: 10.1016/j.mcn.2016.06.007.
653 Beilina, A., Rudenko, I.N., Kaganovich, A., Civiero, L., Chau, H., Kalia, S.K., Kalia, L.V., Lobbestael, E.,
654 Chia, R., Ndukwe, K., Ding, J., Nalls, M.A., International Parkinson's Disease Genomics, C., North
655 American Brain Expression, C., Olszewski, M., Hauser, D.N., Kumaran, R., Lozano, A.M., Baekelandt,
656 V., Greene, L.E., Taymans, J.M., Greggio, E., and Cookson, M.R. (2014). Unbiased screen for
657 interactors of leucine-rich repeat kinase 2 supports a common pathway for sporadic and familial
658 Parkinson disease. *Proceedings of the National Academy of Sciences of the United States of America*
659 *111*, 2626-2631 doi: 10.1073/pnas.1318306111.
660 Bersuker, K., Peterson, C.W.H., To, M., Sahl, S.J., Savikhin, V., Grossman, E.A., Nomura, D.K., and
661 Olzmann, J.A. (2018). A Proximity Labeling Strategy Provides Insights into the Composition and
662 Dynamics of Lipid Droplet Proteomes. *Dev Cell 44*, 97-112 e117 doi: 10.1016/j.devcel.2017.11.020.

663 Boecker, C.A., and Holzbaur, E.L.F. (2021). Hyperactive LRRK2 kinase impairs the trafficking of axonal
664 autophagosomes. *Autophagy 17*, 2043-2045 doi: 10.1080/15548627.2021.1936933.
665 Boldt, K., van Reeuwijk, J., Lu, Q., Koutroumpas, K., Nguyen, T.M., Texier, Y., van Beersum, S.E., Horn,
666 N., Willer, J.R., Mans, D.A., Dougherty, G., Lamers, I.J., Coene, K.L., Arts, H.H., Betts, M.J., Beyer, T.,
667 Bolat, E., Gloeckner, C.J., Haidari, K., Hetterschijt, L., Iaconis, D., Jenkins, D., Klose, F., Knapp, B.*, et*
668 *al.* (2016). An organelle-specific protein landscape identifies novel diseases and molecular
669 mechanisms. *Nature communications 7*, 11491 doi: 10.1038/ncomms11491.
670 Bonet-Ponce, L., Beilina, A., Williamson, C.D., Lindberg, E., Kluss, J.H., Saez-Atienzar, S., Landeck, N.,
671 Kumaran, R., Mamais, A., Bleck, C.K.E., Li, Y., and Cookson, M.R. (2020). LRRK2 mediates tubulation
672 and vesicle sorting from lysosomes. *Sci Adv 6* doi: 10.1126/sciadv.abb2454.
673 Branon, T.C., Bosch, J.A., Sanchez, A.D., Udeshi, N.D., Svinkina, T., Carr, S.A., Feldman, J.L., Perrimon,
674 N., and Ting, A.Y. (2018). Efficient proximity labeling in living cells and organisms with TurboID. *Nat*
675 *Biotechnol 36*, 880-887 doi: 10.1038/nbt.4201.
676 Carrion, M.D.P., Marsicano, S., Daniele, F., Marte, A., Pischedda, F., Di Cairano, E., Piovesana, E., von
677 Zweydorf, F., Kremmer, E., Gloeckner, C.J., Onofri, F., Perego, C., and Piccoli, G. (2017). The LRRK2
678 G2385R variant is a partial loss-of-function mutation that affects synaptic vesicle trafficking through
679 altered protein interactions. *Sci Rep 7*, 5377 doi: 10.1038/s41598-017-05760-9.
680 Chen, C., Xu, Z., Zhang, T., Lin, L., Lu, M., Xie, C., and Yu, X. (2019). Cep85 Relays Plk1 Activity to
681 Phosphorylated Nek2A for Its Timely Activation in Centrosome Disjunction. *iScience 11*, 114-133
682 doi: 10.1016/j.isci.2018.12.013.
683 Cock, P.J., Antao, T., Chang, J.T., Chapman, B.A., Cox, C.J., Dalke, A., Friedberg, I., Hamelryck, T., Kauff,
684 F., Wilczynski, B., and de Hoon, M.J. (2009). Biopython: freely available Python tools for
685 computational molecular biology and bioinformatics. *Bioinformatics 25*, 1422-1423 doi:
686 10.1093/bioinformatics/btp163.
687 Cox, J., Hein, M.Y., Luber, C.A., Paron, I., Nagaraj, N., and Mann, M. (2014). Accurate proteome-wide
688 label-free quantification by delayed normalization and maximal peptide ratio extraction, termed
689 MaxLFQ. *Molecular & cellular proteomics : MCP 13*, 2513-2526 doi: 10.1074/mcp.M113.031591.
690 Deniston, C.K., Salogiannis, J., Mathea, S., Snead, D.M., Lahiri, I., Matyszewski, M., Donosa, O.,
691 Watanabe, R., Bohning, J., Shiau, A.K., Knapp, S., Villa, E., Reck-Peterson, S.L., and Leschziner, A.E.
692 (2020). Structure of LRRK2 in Parkinson's disease and model for microtubule interaction. *Nature*
693 *588*, 344-349 doi: 10.1038/s41586-020-2673-2.
694 Dhekne, H.S., Tonelli, F., Yeshaw, W.M., Chiang, C.Y., Limouse, C., Jaimon, E., Purlyte, E., Alessi, D.R.,
695 and Pfeffer, S.R. (2023). Genome-wide screen reveals Rab12 GTPase as a critical activator of
696 Parkinson's disease-linked LRRK2 kinase. *Elife 12* doi: 10.7554/eLife.87098.

697 Dhekne, H.S., Yanatori, I., Gomez, R.C., Tonelli, F., Diez, F., Schule, B., Steger, M., Alessi, D.R., and
698 Pfeffer, S.R. (2018). A pathway for Parkinson's Disease LRRK2 kinase to block primary cilia and Sonic
699 hedgehog signaling in the brain. *Elife 7* doi: 10.7554/eLife.40202.
700 Dobson-Stone, C., Hallupp, M., Shahheydari, H., Ragagnin, A.M.G., Chatterton, Z., Carew-Jones, F.,
701 Shepherd, C.E., Stefen, H., Paric, E., Fath, T., Thompson, E.M., Blumbergs, P., Short, C.L., Field, C.D.,
702 Panegyres, P.K., Hecker, J., Nicholson, G., Shaw, A.D., Fullerton, J.M., Luty, A.A., Schofield, P.R.,
703 Brooks, W.S., Rajan, N., Bennett, M.F*., et al.* (2020). CYLD is a causative gene for frontotemporal
704 dementia - amyotrophic lateral sclerosis. *Brain 143*, 783-799 doi: 10.1093/brain/awaa039.
705 Doncheva, N.T., Morris, J.H., Gorodkin, J., and Jensen, L.J. (2019). Cytoscape StringApp: Network
706 Analysis and Visualization of Proteomics Data. *Journal of proteome research 18*, 623-632 doi:
707 10.1021/acs.jproteome.8b00702.
708 Douanne, T., Andre-Gregoire, G., Thys, A., Trillet, K., Gavard, J., and Bidere, N. (2019). CYLD Regulates
709 Centriolar Satellites Proteostasis by Counteracting the E3 Ligase MIB1. *Cell Rep 27*, 1657-1665
710 e1654 doi: 10.1016/j.celrep.2019.04.036.
711 Eguether, T., Ermolaeva, M.A., Zhao, Y., Bonnet, M.C., Jain, A., Pasparakis, M., Courtois, G., and Tassin,
712 A.M. (2014). The deubiquitinating enzyme CYLD controls apical docking of basal bodies in ciliated
713 epithelial cells. *Nature communications 5*, 4585 doi: 10.1038/ncomms5585.
714 Ehebauer, M.T., and Arias, A.M. (2009). The structural and functional determinants of the Axin and
715 Dishevelled DIX domains. *BMC Struct Biol 9*, 70 doi: 10.1186/1472-6807-9-70.
716 Evans, R., O'Neill, M., Pritzel, A., Antropova, N., Senior, A., Green, T., Žídek, A., Bates, R., Blackwell, S.,
717 Yim, J., Ronneberger, O., Bodenstein, S., Zielinski, M., Bridgland, A., Potapenko, A., Cowie, A.,
718 Tunyasuvunakool, K., Jain, R., Clancy, E., Kohli, P., Jumper, J., and Hassabis, D. (2021). Protein
719 complex prediction with AlphaFold-Multimer. Preprint available at: *bioRxiv* doi:
720 10.1101/2021.10.04.463034.
721 Fahn, S. (2003). Description of Parkinson's disease as a clinical syndrome. *Annals of the New York*
722 *Academy of Sciences 991*, 1-14 doi: 10.1111/j.1749-6632.2003.tb07458.x.
723 Filippini, F., Nola, S., Zahraoui, A., Roger, K., Esmaili, M., Sun, J., Wojnacki, J., Vlieghe, A., Bun, P.,
724 Blanchon, S., Rain, J.C., Taymans, J.M., Chartier-Harlin, M.C., Guerrera, C., and Galli, T. (2023).
725 Secretion of VGF relies on the interplay between LRRK2 and post-Golgi v-SNAREs. *Cell Rep 42*,
726 112221 doi: 10.1016/j.celrep.2023.112221.
727 Follett, J., and Farrer, M.J. (2021). LRRK2; a dynamic regulator of cellular trafficking. *Brain Res 1761*,
728 147394 doi: 10.1016/j.brainres.2021.147394.
729 Galaxy, C. (2024). The Galaxy platform for accessible, reproducible, and collaborative data analyses:
730 2024 update. *Nucleic acids research 52*, W83-W94 doi: 10.1093/nar/gkae410.

731 Gasser, T., Hardy, J., and Mizuno, Y. (2011). Milestones in PD genetics. *Mov Disord 26*, 1042-1048 doi:
732 10.1002/mds.23637.
733 Geisler, S., Holmstrom, K.M., Skujat, D., Fiesel, F.C., Rothfuss, O.C., Kahle, P.J., and Springer, W. (2010).
734 PINK1/Parkin-mediated mitophagy is dependent on VDAC1 and p62/SQSTM1. *Nat Cell Biol 12*, 119-
735 131 doi: 10.1038/ncb2012.
736 Gloeckner, C.J., Boldt, K., Schumacher, A., Roepman, R., and Ueffing, M. (2007). A novel tandem affinity
737 purification strategy for the efficient isolation and characterisation of native protein complexes.
738 *Proteomics 7*, 4228-4234 doi: 10.1002/pmic.200700038.
739 Gloeckner, C.J., Boldt, K., and Ueffing, M. (2009). Strep/FLAG tandem affinity purification (SF-TAP) to
740 study protein interactions. *Current protocols in protein science / editorial board, John E Coligan [et*
741 *al] Chapter 19*, Unit19 20 doi: 10.1002/0471140864.ps1920s57.
742 Gloeckner, C.J., and Porras, P. (2020). Guilt-by-Association - Functional Insights Gained From Studying
743 the LRRK2 Interactome. *Front Neurosci 14*, 485 doi: 10.3389/fnins.2020.00485.
744 Grishin, N.V. (2001). KH domain: one motif, two folds. *Nucleic acids research 29*, 638-643 doi:
745 10.1093/nar/29.3.638.
746 Guaitoli, G., Raimondi, F., Gilsbach, B.K., Gomez-Llorente, Y., Deyaert, E., Renzi, F., Li, X., Schaffner, A.,
747 Jagtap, P.K., Boldt, K., von Zweydorf, F., Gotthardt, K., Lorimer, D.D., Yue, Z., Burgin, A., Janjic, N.,
748 Sattler, M., Versees, W., Ueffing, M., Ubarretxena-Belandia, I., Kortholt, A., and Gloeckner, C.J.
749 (2016). Structural model of the dimeric Parkinson's protein LRRK2 reveals a compact architecture
750 involving distant interdomain contacts. *Proceedings of the National Academy of Sciences of the*
751 *United States of America 113*, E4357-4366 doi: 10.1073/pnas.1523708113.
752 Guaitoli, G., Zhang, X., Saitta, F., Miglionico, P., Silbermann, L.M., Ho, F.Y., von Zweydorf, F., Signorelli,
753 M., Tych, K., Fessas, D., Raimondi, F., Kortholt, A., and Gloeckner, C.J. (2023). Biophysical analysis
754 reveals autophosphorylation as an important regulator of LRRK2 dimerization. Preprint available at:
755 *bioRxiv* doi: 10.1101/2023.08.11.549911.
756 Hall, E.A., Kumar, D., Prosser, S.L., Yeyati, P.L., Herranz-Perez, V., Garcia-Verdugo, J.M., Rose, L., McKie,
757 L., Dodd, D.O., Tennant, P.A., Megaw, R., Murphy, L.C., Ferreira, M.F., Grimes, G., Williams, L.,
758 Quidwai, T., Pelletier, L., Reiter, J.F., and Mill, P. (2023). Centriolar satellites expedite mother
759 centriole remodeling to promote ciliogenesis. *Elife 12* doi: 10.7554/eLife.79299.
760 Hallett, P.J., Engelender, S., and Isacson, O. (2019). Lipid and immune abnormalities causing age-
761 dependent neurodegeneration and Parkinson's disease. *J Neuroinflammation 16*, 153 doi:
762 10.1186/s12974-019-1532-2.
763 Hori, A., and Toda, T. (2017). Regulation of centriolar satellite integrity and its physiology. *Cellular and*
764 *molecular life sciences : CMLS 74*, 213-229 doi: 10.1007/s00018-016-2315-x.

765 Islam, M.S., Nolte, H., Jacob, W., Ziegler, A.B., Putz, S., Grosjean, Y., Szczepanowska, K., Trifunovic, A.,
766 Braun, T., Heumann, H., Heumann, R., Hovemann, B., Moore, D.J., and Kruger, M. (2016). Human
767 R1441C LRRK2 regulates the synaptic vesicle proteome and phosphoproteome in a Drosophila
768 model of Parkinson's disease. *Human molecular genetics 25*, 5365-5382 doi: 10.1093/hmg/ddw352.
769 Jennings, D., Huntwork-Rodriguez, S., Henry, A.G., Sasaki, J.C., Meisner, R., Diaz, D., Solanoy, H., Wang,
770 X., Negrou, E., Bondar, V.V., Ghosh, R., Maloney, M.T., Propson, N.E., Zhu, Y., Maciuca, R.D., Harris,
771 L., Kay, A., LeWitt, P., King, T.A., Kern, D., Ellenbogen, A., Goodman, I., Siderowf, A., Aldred, J*., et al.*
772 (2022). Preclinical and clinical evaluation of the LRRK2 inhibitor DNL201 for Parkinson's disease.
773 *Science translational medicine 14*, eabj2658 doi: 10.1126/scitranslmed.abj2658.
774 Jian, F., Wang, S., Tian, R., Wang, Y., Li, C., Li, Y., Wang, S., Fang, C., Ma, C., and Rong, Y. (2024). The
775 STX17-SNAP47-VAMP7/VAMP8 complex is the default SNARE complex mediating autophagosome-
776 lysosome fusion. *Cell Res* doi: 10.1038/s41422-023-00916-x.
777 Kafka, A., Basic-Kinda, S., and Pecina-Slaus, N. (2014). The cellular story of dishevelleds. *Croat Med J*
778 *55*, 459-467 doi: 10.3325/cmj.2014.55.459.
779 Kaleb, K., Vesztrocy, A.W., Altenhoff, A., and Dessimoz, C. (2019). Expanding the Orthologous Matrix
780 (OMA) programmatic interfaces: REST API and the OmaDB packages for R and Python. *F1000Res 8*,
781 42 doi: 10.12688/f1000research.17548.2.
782 Kalogeropulou, A.F., Purlyte, E., Tonelli, F., Lange, S.M., Wightman, M., Prescott, A.R., Padmanabhan,
783 S., Sammler, E., and Alessi, D.R. (2022). Impact of 100 LRRK2 variants linked to Parkinson's Disease
784 on kinase activity and microtubule binding. *The Biochemical journal* doi: 10.1042/BCJ20220161.
785 Kalogeropulou, A.F., Zhao, J., Bolliger, M.F., Memou, A., Narasimha, S., Molitor, T.P., Wilson, W.H.,
786 Rideout, H.J., and Nichols, R.J. (2018). P62/SQSTM1 is a novel leucine-rich repeat kinase 2 (LRRK2)
787 substrate that enhances neuronal toxicity. *The Biochemical journal 475*, 1271-1293 doi:
788 10.1042/BCJ20170699.
789 Kanao, T., Venderova, K., Park, D.S., Unterman, T., Lu, B., and Imai, Y. (2010). Activation of FoxO by
790 LRRK2 induces expression of proapoptotic proteins and alters survival of postmitotic dopaminergic
791 neuron in Drosophila. *Human molecular genetics 19*, 3747-3758 doi: 10.1093/hmg/ddq289.
792 Khan, S.S., Jaimon, E., Lin, Y.E., Nikoloff, J., Tonelli, F., Alessi, D.R., and Pfeffer, S.R. (2024). Loss of
793 primary cilia and dopaminergic neuroprotection in pathogenic LRRK2-driven and idiopathic
794 Parkinson's disease. Preprint available at: *bioRxiv* doi: 10.1101/2024.01.15.575737.
795 Kiel, C., Vogt, A., Campagna, A., Chatr-aryamontri, A., Swiatek-de Lange, M., Beer, M., Bolz, S., Mack,
796 A.F., Kinkl, N., Cesareni, G., Serrano, L., and Ueffing, M. (2011). Structural and functional protein
797 network analyses predict novel signaling functions for rhodopsin. *Molecular systems biology 7*, 551
798 doi: 10.1038/msb.2011.83.

799 Kim, D.I., Jensen, S.C., Noble, K.A., Kc, B., Roux, K.H., Motamedchaboki, K., and Roux, K.J. (2016). An
800 improved smaller biotin ligase for BioID proximity labeling. *Mol Biol Cell 27*, 1188-1196 doi:
801 10.1091/mbc.E15-12-0844.
802 Kluss, J.H., Bonet-Ponce, L., Lewis, P.A., and Cookson, M.R. (2022a). Directing LRRK2 to membranes of
803 the endolysosomal pathway triggers RAB phosphorylation and JIP4 recruitment. *Neurobiol Dis 170*,
804 105769 doi: 10.1016/j.nbd.2022.105769.
805 Kluss, J.H., Lewis, P.A., and Greggio, E. (2022b). Leucine-rich repeat kinase 2 (LRRK2): an update on the
806 potential therapeutic target for Parkinson's disease. *Expert Opin Ther Targets 26*, 537-546 doi:
807 10.1080/14728222.2022.2082937.
808 Kucera, M., Isserlin, R., Arkhangorodsky, A., and Bader, G.D. (2016). AutoAnnotate: A Cytoscape app
809 for summarizing networks with semantic annotations. *F1000Res 5*, 1717 doi:
810 10.12688/f1000research.9090.1.
811 Kumar, M., Acevedo-Cintron, J., Jhaldiyal, A., Wang, H., Andrabi, S.A., Eacker, S., Karuppagounder, S.S.,
812 Brahmachari, S., Chen, R., Kim, H., Ko, H.S., Dawson, V.L., and Dawson, T.M. (2020). Defects in
813 Mitochondrial Biogenesis Drive Mitochondrial Alterations in PARKIN-Deficient Human Dopamine
814 Neurons. *Stem Cell Reports 15*, 629-645 doi: 10.1016/j.stemcr.2020.07.013.
815 Lara Ordonez, A.J., Fasiczka, R., Fernandez, B., Naaldijk, Y., Fdez, E., Blanca Ramirez, M., Phan, S.,
816 Boassa, D., and Hilfiker, S. (2022). The LRRK2 signaling network converges on a centriolar phospho-
817 Rab10/RILPL1 complex to cause deficits in centrosome cohesion and cell polarization. *Biol Open 11*
818 doi: 10.1242/bio.059468.
819 Lara Ordonez, A.J., Fernandez, B., Fdez, E., Romo-Lozano, M., Madero-Perez, J., Lobbestael, E.,
820 Baekelandt, V., Aiastui, A., Lopez de Munain, A., Melrose, H.L., Civiero, L., and Hilfiker, S. (2019).
821 RAB8, RAB10 and RILPL1 contribute to both LRRK2 kinase-mediated centrosomal cohesion and
822 ciliogenesis deficits. *Human molecular genetics 28*, 3552-3568 doi: 10.1093/hmg/ddz201.
823 Li, B.J., Chen, H., Jiang, S.S., Wang, C.Y., Tuo, Q.H., Long, S.Y., Zhang, C.P., and Liao, D.F. (2020). PX
824 Domain-Containing Kinesin KIF16B and Microtubule-Dependent Intracellular Movements. *J Membr*
825 *Biol 253*, 101-108 doi: 10.1007/s00232-020-00110-9.
826 Li, X., Zhu, H., Huang, B.T., Li, X., Kim, H., Tan, H., Zhang, Y., Choi, I., Peng, J., Xu, P., Sun, J., and Yue, Z.
827 (2024). RAB12-LRRK2 Complex Suppresses Primary Ciliogenesis and Regulates Centrosome
828 Homeostasis in Astrocytes. Preprint available at: *bioRxiv*, 2024.2007.2017.603999 doi:
829 10.1101/2024.07.17.603999.
830 Lim, K.L., Chew, K.C., Tan, J.M., Wang, C., Chung, K.K., Zhang, Y., Tanaka, Y., Smith, W., Engelender, S.,
831 Ross, C.A., Dawson, V.L., and Dawson, T.M. (2005). Parkin mediates nonclassical, proteasomal-
832 independent ubiquitination of synphilin-1: implications for Lewy body formation. *J Neurosci 25*,
833 2002-2009 doi: 10.1523/JNEUROSCI.4474-04.2005.

834 Liu, X., Salokas, K., Weldatsadik, R.G., Gawriyski, L., and Varjosalo, M. (2020). Combined proximity
835 labeling and affinity purification-mass spectrometry workflow for mapping and visualizing protein
836 interaction networks. *Nature protocols 15*, 3182-3211 doi: 10.1038/s41596-020-0365-x.
837 Manzoni, C., Denny, P., Lovering, R.C., and Lewis, P.A. (2015). Computational analysis of the LRRK2
838 interactome. *PeerJ 3*, e778 doi: 10.7717/peerj.778.
839 Matic, M., Miglionico, P., Tatsumi, M., Inoue, A., and Raimondi, F. (2023). GPCRome-wide analysis of
840 G-protein-coupling diversity using a computational biology approach. *Nature communications 14*,
841 4361 doi: 10.1038/s41467-023-40045-y.
842 McGrath, E., Waschbusch, D., Baker, B.M., and Khan, A.R. (2021). LRRK2 binds to the Rab32 subfamily
843 in a GTP-dependent manner via its armadillo domain. *Small GTPases 12*, 133-146 doi:
844 10.1080/21541248.2019.1666623.
845 Meixner, A., Boldt, K., Van Troys, M., Askenazi, M., Gloeckner, C.J., Bauer, M., Marto, J.A., Ampe, C.,
846 Kinkl, N., and Ueffing, M. (2011). A QUICK screen for Lrrk2 interaction partners--leucine-rich repeat
847 kinase 2 is involved in actin cytoskeleton dynamics. *Molecular & cellular proteomics : MCP 10*, M110
848 001172 doi: 10.1074/mcp.M110.001172.
849 Meldal, B.H.M., Perfetto, L., Combe, C., Lubiana, T., Ferreira Cavalcante, J.V., Bye, A.J.H., Waagmeester,
850 A., Del-Toro, N., Shrivastava, A., Barrera, E., Wong, E., Mlecnik, B., Bindea, G., Panneerselvam, K.,
851 Willighagen, E., Rappsilber, J., Porras, P., Hermjakob, H., and Orchard, S. (2022). Complex Portal
852 2022: new curation frontiers. *Nucleic acids research 50*, D578-D586 doi: 10.1093/nar/gkab991.
853 Mellacheruvu, D., Wright, Z., Couzens, A.L., Lambert, J.P., St-Denis, N.A., Li, T., Miteva, Y.V., Hauri, S.,
854 Sardiu, M.E., Low, T.Y., Halim, V.A., Bagshaw, R.D., Hubner, N.C., Al-Hakim, A., Bouchard, A.,
855 Faubert, D., Fermin, D., Dunham, W.H., Goudreault, M., Lin, Z.Y., Badillo, B.G., Pawson, T., Durocher,
856 D., Coulombe, B*., et al.* (2013). The CRAPome: a contaminant repository for affinity purification-
857 mass spectrometry data. *Nature methods 10*, 730-736 doi: 10.1038/nmeth.2557.
858 Miglionico, P., Nemati Fard, L.A., Gloeckner, C.J., and Raimondi, F. (2024, in prep.). Predicition and
859 discovery of protein-protein direct interactions and stable complexes based on gene co-expression
860 and co-evolution. *bioRxiv*, preprint in preparation.
861 Miller, G.K., Kuruvilla, S., Jacob, B., LaFranco-Scheuch, L., Bakthavatchalu, V., Flor, J., Flor, K., Ziegler,
862 J., Reichard, C., Manfre, P., Firner, S., McNutt, T., Quay, D., Bellum, S., Doto, G., Ciaccio, P.J.,
863 Pearson, K., Valentine, J., Fuller, P., Fell, M., Tsuchiya, T., Williamson, T., and Wollenberg, G. (2023).
864 Effects of LRRK2 Inhibitors in Nonhuman Primates. *Toxicol Pathol*, 1926233231205895 doi:
865 10.1177/01926233231205895.
866 Mohd Rafiq, N., Fujise, K., Rosenfeld, M.S., Xu, P., and De Camilli, P. (2024). Parkinsonism Sac domain
867 mutation in Synaptojanin-1 affects ciliary properties in iPSC-derived dopaminergic neurons.

Proceedings of the National Academy of Sciences of the United States of America 121, e2318943121 doi: 10.1073/pnas.2318943121.

Moreira, C., Kelemen, C.D., Obado, S.O., Zahedifard, F., Zhang, N., Holetz, F.B., Gauglitz, L., Dallagiovanna, B., Field, M.C., Kramer, S., and Zoltner, M. (2023). Impact of inherent biases built into proteomic techniques: Proximity labeling and affinity capture compared. *The Journal of biological chemistry 299*, 102726 doi: 10.1016/j.jbc.2022.102726.

Myasnikov, A., Zhu, H., Hixson, P., Xie, B., Yu, K., Pitre, A., Peng, J., and Sun, J. (2021). Structural analysis of the full-length human LRRK2. *Cell 184*, 3519-3527 e3510 doi: 10.1016/j.cell.2021.05.004.

Naaldijk, Y., Fernandez, B., Fasiczka, R., Fdez, E., Leghay, C., Croitoru, I., Kwok, J.B., Boulesnane, Y., Vizeneux, A., Mutez, E., Calvez, C., Destee, A., Taymans, J.M., Aragon, A.V., Yarza, A.B., Padmanabhan, S., Delgado, M., Alcalay, R.N., Chatterton, Z., Dzamko, N., Halliday, G., Ruiz-Martinez, J., Chartier-Harlin, M.C., and Hilfiker, S. (2024). A potential patient stratification biomarker for Parkinson s disease based on LRRK2 kinase-mediated centrosomal alterations in peripheral blood-derived cells. *NPJ Parkinsons Dis 10*, 12 doi: 10.1038/s41531-023-00624-8.

Orchard, S., Ammari, M., Aranda, B., Breuza, L., Briganti, L., Broackes-Carter, F., Campbell, N.H., Chavali, G., Chen, C., del-Toro, N., Duesbury, M., Dumousseau, M., Galeota, E., Hinz, U., Iannuccelli, M., Jagannathan, S., Jimenez, R., Khadake, J., Lagreid, A., Licata, L., Lovering, R.C., Meldal, B., Melidoni, A.N., Milagros, M*., et al.* (2014). The MIntAct project--IntAct as a common curation platform for 11 molecular interaction databases. *Nucleic acids research 42*, D358-363 doi: 10.1093/nar/gkt1115.

Paisan-Ruiz, C., Jain, S., Evans, E.W., Gilks, W.P., Simon, J., van der Brug, M., Lopez de Munain, A., Aparicio, S., Gil, A.M., Khan, N., Johnson, J., Martinez, J.R., Nicholl, D., Marti Carrera, I., Pena, A.S., de Silva, R., Lees, A., Marti-Masso, J.F., Perez-Tur, J., Wood, N.W., and Singleton, A.B. (2004). Cloning of the gene containing mutations that cause PARK8-linked Parkinson's disease. *Neuron 44*, 595-600 doi: 10.1016/j.neuron.2004.10.023.

Park, S., Han, S., Choi, I., Kim, B., Park, S.P., Joe, E.H., and Suh, Y.H. (2016). Interplay between Leucine-Rich Repeat Kinase 2 (LRRK2) and p62/SQSTM-1 in Selective Autophagy. *PloS one 11*, e0163029 doi: 10.1371/journal.pone.0163029.

Pedregosa, F., Varoquaux, G., Gramfort, A., Michel, V., B., T., Griesel, O., Blondel, M., Prettenhofer, P., Weiss, R., Dubourg, V., Vanderplas, J., Passos, A., D., C., M., B., Perrot, M., and E., D. (2011). Scikit-learn: Machine Learning in Python. *Journal of Machine Learning Research 12*, 2825-2830 doi:

Perez-Riverol, Y., Bai, J., Bandla, C., Garcia-Seisdedos, D., Hewapathirana, S., Kamatchinathan, S., Kundu, D.J., Prakash, A., Frericks-Zipper, A., Eisenacher, M., Walzer, M., Wang, S., Brazma, A., and Vizcaino, J.A. (2022). The PRIDE database resources in 2022: a hub for mass spectrometry-based proteomics evidences. *Nucleic acids research 50*, D543-D552 doi: 10.1093/nar/gkab1038.

903 Piccoli, G., Condliffe, S.B., Bauer, M., Giesert, F., Boldt, K., De Astis, S., Meixner, A., Sarioglu, H., Vogt-
904 Weisenhorn, D.M., Wurst, W., Gloeckner, C.J., Matteoli, M., Sala, C., and Ueffing, M. (2011). LRRK2
905 controls synaptic vesicle storage and mobilization within the recycling pool. *J Neurosci 31*, 2225-
906 2237 doi: 10.1523/JNEUROSCI.3730-10.2011.
907 Piccoli, G., Onofri, F., Cirnaru, M.D., Kaiser, C.J., Jagtap, P., Kastenmuller, A., Pischedda, F., Marte, A.,
908 von Zweydorf, F., Vogt, A., Giesert, F., Pan, L., Antonucci, F., Kiel, C., Zhang, M., Weinkauf, S., Sattler,
909 M., Sala, C., Matteoli, M., Ueffing, M., and Gloeckner, C.J. (2014). Leucine-rich repeat kinase 2 binds
910 to neuronal vesicles through protein interactions mediated by its C-terminal WD40 domain. *Mol*
911 *Cell Biol 34*, 2147-2161 doi: 10.1128/MCB.00914-13.
912 Pirooznia, S.K., Wang, H., Panicker, N., Kumar, M., Neifert, S., Dar, M.A., Lau, E., Kang, B.G., Redding-
913 Ochoa, J., Troncoso, J.C., Dawson, V.L., and Dawson, T.M. (2022). Deubiquitinase CYLD acts as a
914 negative regulator of dopamine neuron survival in Parkinson's disease. *Sci Adv 8*, eabh1824 doi:
915 10.1126/sciadv.abh1824.
916 Prosser, S.L., Tkach, J., Gheiratmand, L., Kim, J., Raught, B., Morrison, C.G., and Pelletier, L. (2022).
917 Aggresome assembly at the centrosome is driven by CP110-CEP97-CEP290 and centriolar satellites.
918 *Nat Cell Biol 24*, 483-496 doi: 10.1038/s41556-022-00869-0.
919 Purlyte, E., Dhekne, H.S., Sarhan, A.R., Gomez, R., Lis, P., Wightman, M., Martinez, T.N., Tonelli, F.,
920 Pfeffer, S.R., and Alessi, D.R. (2018). Rab29 activation of the Parkinson's disease-associated LRRK2
921 kinase. *The EMBO journal 37*, 1-18 doi: 10.15252/embj.201798099.
922 Qin, W., Cho, K.F., Cavanagh, P.E., and Ting, A.Y. (2021). Deciphering molecular interactions by
923 proximity labeling. *Nature methods 18*, 133-143 doi: 10.1038/s41592-020-01010-5.
924 Ragueneau, E., Shrivastava, A., Morris, J.H., Del-Toro, N., Hermjakob, H., and Porras, P. (2021). IntAct
925 App: a Cytoscape application for molecular interaction network visualization and analysis.
926 *Bioinformatics 37*, 3684-3685 doi: 10.1093/bioinformatics/btab319.
927 Raig, N.D., Surridge, K.J., Sanz-Murillo, M., Dederer, V., Kramer, A., Schwalm, M.P., Elson, L., Chatterjee,
928 D., Mathea, S., Hanke, T., Leschziner, A.E., Reck-Peterson, S.L., and Knapp, S. (2024). Type-II kinase
929 inhibitors that target Parkinson's Disease-associated LRRK2. Preprint available at: *bioRxiv*,
930 2024.2009.2017.613365 doi: 10.1101/2024.09.17.613365.
931 Rousseeuw, P.J. (1987). Silhouettes: A graphical aid to the interpretation and validation of cluster
932 analysis. *Journal of Computational and Applied Mathematics 20*, 53-65 doi: 10.1016/0377-
933 0427(87)90125-7.
934 Roux, K.J., Kim, D.I., Raida, M., and Burke, B. (2012). A promiscuous biotin ligase fusion protein
935 identifies proximal and interacting proteins in mammalian cells. *J Cell Biol 196*, 801-810 doi:
936 10.1083/jcb.201112098.

937 Sancho, R.M., Law, B.M., and Harvey, K. (2009). Mutations in the LRRK2 Roc-COR tandem domain link
938 Parkinson's disease to Wnt signalling pathways. *Human molecular genetics 18*, 3955-3968 doi:
939 10.1093/hmg/ddp337.
940 Schmidt, S., Luecken, M.D., Trumbach, D., Hembach, S., Niedermeier, K.M., Wenck, N., Pflugler, K.,
941 Stautner, C., Bottcher, A., Lickert, H., Ramirez-Suastegui, C., Ahmad, R., Ziller, M.J., Fitzgerald, J.C.,
942 Ruf, V., van de Berg, W.D.J., Jonker, A.J., Gasser, T., Winner, B., Winkler, J., Vogt Weisenhorn, D.M.,
943 Giesert, F., Theis, F.J., and Wurst, W. (2022). Primary cilia and SHH signaling impairments in human
944 and mouse models of Parkinson's disease. *Nature communications 13*, 4819 doi: 10.1038/s41467-
945 022-32229-9.
946 Shannon, P., Markiel, A., Ozier, O., Baliga, N.S., Wang, J.T., Ramage, D., Amin, N., Schwikowski, B., and
947 Ideker, T. (2003). Cytoscape: a software environment for integrated models of biomolecular
948 interaction networks. *Genome Res 13*, 2498-2504 doi: 10.1101/gr.1239303.
949 Shin, W.H., Park, J.H., and Chung, K.C. (2020). The central regulator p62 between ubiquitin proteasome
950 system and autophagy and its role in the mitophagy and Parkinson's disease. *BMB Rep 53*, 56-63
951 doi: 10.5483/BMBRep.2020.53.1.283.
952 Simon-Sanchez, J., Schulte, C., Bras, J.M., Sharma, M., Gibbs, J.R., Berg, D., Paisan-Ruiz, C., Lichtner, P.,
953 Scholz, S.W., Hernandez, D.G., Kruger, R., Federoff, M., Klein, C., Goate, A., Perlmutter, J., Bonin,
954 M., Nalls, M.A., Illig, T., Gieger, C., Houlden, H., Steffens, M., Okun, M.S., Racette, B.A., Cookson,
955 M.R.*, et al.* (2009). Genome-wide association study reveals genetic risk underlying Parkinson's
956 disease. *Nat Genet 41*, 1308-1312 doi: 10.1038/ng.487.
957 Sowa, M.E., Bennett, E.J., Gygi, S.P., and Harper, J.W. (2009). Defining the human deubiquitinating
958 enzyme interaction landscape. *Cell 138*, 389-403 doi: 10.1016/j.cell.2009.04.042.
959 Steger, M., Diez, F., Dhekne, H.S., Lis, P., Nirujogi, R.S., Karayel, O., Tonelli, F., Martinez, T.N., Lorentzen,
960 E., Pfeffer, S.R., Alessi, D.R., and Mann, M. (2017). Systematic proteomic analysis of LRRK2-
961 mediated Rab GTPase phosphorylation establishes a connection to ciliogenesis. *Elife 6* doi:
962 10.7554/eLife.31012.
963 Stevens, D.A., Lee, Y., Kang, H.C., Lee, B.D., Lee, Y.I., Bower, A., Jiang, H., Kang, S.U., Andrabi, S.A.,
964 Dawson, V.L., Shin, J.H., and Dawson, T.M. (2015). Parkin loss leads to PARIS-dependent declines in
965 mitochondrial mass and respiration. *Proceedings of the National Academy of Sciences of the United*
966 *States of America 112*, 11696-11701 doi: 10.1073/pnas.1500624112.
967 Tasegian, A., Singh, F., Ganley, I.G., Reith, A.D., and Alessi, D.R. (2021). Impact of Type II LRRK2
968 inhibitors on signaling and mitophagy. *The Biochemical journal 478*, 3555-3573 doi:
969 10.1042/BCJ20210375.

970 Taylor, S.S., Kaila-Sharma, P., Weng, J.H., Aoto, P., Schmidt, S.H., Knapp, S., Mathea, S., and Herberg,
971 F.W. (2020). Kinase Domain Is a Dynamic Hub for Driving LRRK2 Allostery. *Frontiers in molecular*
972 *neuroscience 13*, 538219 doi: 10.3389/fnmol.2020.538219.
973 Teo, G., Liu, G., Zhang, J., Nesvizhskii, A.I., Gingras, A.C., and Choi, H. (2014). SAINTexpress:
974 improvements and additional features in Significance Analysis of INTeractome software. *J*
975 *Proteomics 100*, 37-43 doi: 10.1016/j.jprot.2013.10.023.
976 Tollenaere, M.A.X., Villumsen, B.H., Blasius, M., Nielsen, J.C., Wagner, S.A., Bartek, J., Beli, P., Mailand,
977 N., and Bekker-Jensen, S. (2015). p38- and MK2-dependent signalling promotes stress-induced
978 centriolar satellite remodelling via 14-3-3-dependent sequestration of CEP131/AZI1. *Nature*
979 *communications 6*, 10075 doi: 10.1038/ncomms10075.
980 Treier, M., Staszewski, L.M., and Bohmann, D. (1994). Ubiquitin-dependent c-Jun degradation in vivo
981 is mediated by the delta domain. *Cell 78*, 787-798 doi: 10.1016/s0092-8674(94)90502-9.
982 Tyanova, S., Temu, T., Sinitcyn, P., Carlson, A., Hein, M.Y., Geiger, T., Mann, M., and Cox, J. (2016). The
983 Perseus computational platform for comprehensive analysis of (prote)omics data. *Nature methods*
984 *13*, 731-740 doi: 10.1038/nmeth.3901.
985 Vides, E.G., Adhikari, A., Chiang, C.Y., Lis, P., Purlyte, E., Limouse, C., Shumate, J.L., Spinola-Lasso, E.,
986 Dhekne, H.S., Alessi, D.R., and Pfeffer, S.R. (2022). A feed-forward pathway drives LRRK2 kinase
987 membrane recruitment and activation. *Elife 11* doi: 10.7554/eLife.79771.
988 Waschbusch, D., Michels, H., Strassheim, S., Ossendorf, E., Kessler, D., Gloeckner, C.J., and Barnekow,
989 A. (2014). LRRK2 transport is regulated by its novel interacting partner Rab32. *PloS one 9*, e111632
990 doi: 10.1371/journal.pone.0111632.
991 Wauters, L., Versees, W., and Kortholt, A. (2019). Roco Proteins: GTPases with a Baroque Structure and
992 Mechanism. *Int J Mol Sci 20* doi: 10.3390/ijms20010147.
993 Wilhelm, L.P., Zapata-Munoz, J., Villarejo-Zori, B., Pellegrin, S., Freire, C.M., Toye, A.M., Boya, P., and
994 Ganley, I.G. (2022). BNIP3L/NIX regulates both mitophagy and pexophagy. *The EMBO journal 41*,
995 e111115 doi: 10.15252/embj.2022111115.
996 Xue, J., Zhang, J., Zhang, J., Liu, J., Wang, F., Li, K., and Liu, C. (2023). The Parkinson's disease-associated
997 mutation LRRK2 G2385R alters mitochondrial biogenesis via the PGC-1alpha-TFAM pathway.
998 *Mitochondrion 73*, 10-18 doi: 10.1016/j.mito.2023.09.002.
999 Yang, Y., Ran, J., Liu, M., Li, D., Li, Y., Shi, X., Meng, D., Pan, J., Ou, G., Aneja, R., Sun, S.C., and Zhou, J.
1000 (2014). CYLD mediates ciliogenesis in multiple organs by deubiquitinating Cep70 and inactivating
1001 HDAC6. *Cell Res 24*, 1342-1353 doi: 10.1038/cr.2014.136.
1002 Yu, M., Arshad, M., Wang, W., Zhao, D., Xu, L., and Zhou, L. (2018). LRRK2 mediated Rab8a
1003 phosphorylation promotes lipid storage. *Lipids Health Dis 17*, 34 doi: 10.1186/s12944-018-0684-x.

1004 Zhao, Y., Bracher-Smith, M., Li, Y., Harvey, K., Escott-Price, V., Lewis, P.A., and Manzoni, C. (2024).
1005 Transcriptomics and weighted protein network analyses of the LRRK2 protein interactome reveal
1006 distinct molecular signatures for sporadic and LRRK2 Parkinson's Disease. *NPJ Parkinsons Dis 10*,
1007 144 doi: 10.1038/s41531-024-00761-8.
1008 Zhao, Y., Vavouraki, N., Lovering, R.C., Escott-Price, V., Harvey, K., Lewis, P.A., and Manzoni, C. (2023).
1009 Tissue specific LRRK2 interactomes reveal a distinct striatal functional unit. *PLoS Comput Biol 19*,
1010 e1010847 doi: 10.1371/journal.pcbi.1010847.
1011 Zheng, L., Bernard-Marissal, N., Moullan, N., D'Amico, D., Auwerx, J., Moore, D.J., Knott, G., Aebischer,
1012 P., and Schneider, B.L. (2017). Parkin functionally interacts with PGC-1α to preserve mitochondria
1013 and protect dopaminergic neurons. *Human molecular genetics 26*, 582-598 doi:
1014 10.1093/hmg/ddw418.
1015 Zhu, H., Hixson, P., Ma, W., and Sun, J. (2024). Pharmacology of LRRK2 with type I and II kinase
1016 inhibitors revealed by cryo-EM. *Cell Discov 10*, 10 doi: 10.1038/s41421-023-00639-8.
1017 Zhu, H., Tonelli, F., Turk, M., Prescott, A., Alessi, D.R., and Sun, J. (2023). Rab29-dependent
1018 asymmetrical activation of leucine-rich repeat kinase 2. *Science 382*, 1404-1411 doi:
1019 10.1126/science.adi9926.
1020 Zimprich, A., Biskup, S., Leitner, P., Lichtner, P., Farrer, M., Lincoln, S., Kachergus, J., Hulihan, M., Uitti,
1021 R.J., Calne, D.B., Stoessl, A.J., Pfeiffer, R.F., Patenge, N., Carbajal, I.C., Vieregge, P., Asmus, F., Muller-
1022 Myhsok, B., Dickson, D.W., Meitinger, T., Strom, T.M., Wszolek, Z.K., and Gasser, T. (2004).
1023 Mutations in LRRK2 cause autosomal-dominant parkinsonism with pleomorphic pathology. *Neuron*
1024 *44*, 601-607 doi: 10.1016/j.neuron.2004.11.005.

1025 **Tables:**

Accession	Gene name	Protein name	Jaccard score
Q5S007	LRRK2	Leucine-rich repeat serine/threonine-protein kinase 2 (bait)	1.000000
Q9NQC7	**CYLD**	**Ubiquitin carboxyl-terminal hydrolase CYLD**	**0.848485**
Q6P2H3	CEP85	Centrosomal protein of 85 kDa	0.846626
Q96JH7	VCPIP1	Deubiquitinating protein VCPIP1	0.834286
Q96L93	KIF16B	Kinesin-like protein KIF16B	0.832335
P78312	FAM193A	Protein FAM193A	0.817647
Q8NEY1	NAV1	Neuron navigator 1	0.817073
Q7Z2T5	TRMT1L	TRMT1-like protein	0.815951
Q5SZL2	CEP85L	Centrosomal protein of 85 kDa-like	0.810127
O95684	CEP43	Centrosomal protein 43	0.809816
Q96RS0	TGS1	Trimethylguanosine synthase	0.798742

1026

1027 **Table 1:** 10 IDs with the highest Jaccard score underlying identified “Cluster 2”. The DUB CYLD (bold)
1028 shows highest co-evolution to LRRK2.

1029

1030

Accession	Protein name	Gene name	p-value	Log2 T-test difference
P81605	Dermcidin	DCD	2.91844	3.3
Q9UPN4	Centrosomal protein of 131 kDa	CEP131	4.15494	2.2
Q49A88	Coiled-coil domain-containing protein 14	CCDC14	5.39373	2.1
Q9Y2D8	Afadin- and alpha-actinin-binding protein	SSX2IP	2.98866	2.1
O75665	Oral-facial-digital syndrome 1 protein	OFD1	7.92350	2.0
Q15154	Pericentriolar material 1 protein	PCM1	6.62987	1.8
Q9UHB6	LIM domain and actin-binding protein 1	LIMA1	2.96451	1.7
Q8WXW3	Progesterone-induced-blocking factor 1	PIBF1	4.62801	1.5
Q6WCQ1	Myosin phosphatase Rho-interacting protein	MPRIP	7.40967	1.5
Q14596	Next to BRCA1 gene 1 protein	NBR1	3.34347	1.3
Q5TB80	Centrosomal protein of 162 kDa	CEP162	3.46643	1.3
Q8WWI1	LIM domain only protein 7	LMO7	5.84664	1.3

1031

1032 **Table 2:** Enriched proteins in the LRRK2 proximity proteome upon MLi-2 treatment (FDR-controlled T-
1033 test).

1034

Accession	Protein name	Gene name	p-value (-log10)	Log2 T-test difference
O14966	Ras-related protein Rab-7L1	RAB29	9,72545	10,5
Q8IZA0	Dyslexia-associated protein KIAA0319-like protein	KIAA0319L	5,00209	4,9
Q6WKZ4	Rab11 family-interacting protein 1	RAB11FIP1	4,56815	4,6
O15126	Secretory carrier-associated membrane protein 1	SCAMP1	4,09385	3,5
Q9UIQ6	Leucyl-cystinyl aminopeptidase;Leucyl-cystinyl aminopeptidase, pregnancy serum form	LNPEP	4,33552	3,4
Q9H2J7	Sodium-dependent neutral amino acid transporter B(0)AT2	SLC6A15	5,06972	2,9
Q96QD8	Sodium-coupled neutral amino acid transporter 2	SLC38A2	2,89271	2,9
Q13586	Stromal interaction molecule 1	STIM1	3,12115	2,8
P98194	Calcium-transporting ATPase type 2C member 1	ATP2C1	5,00347	2,6
Q9H2H9	Sodium-coupled neutral amino acid transporter 1	SLC38A1	2,37723	2,6
O75976	Carboxypeptidase D	CPD	3,20952	2,6
Q14126	Desmoglein-2	DSG2	4,31421	2,5
P51809	Vesicle-associated membrane protein 7	VAMP7	4,02209	2,5
Q8NDI1	EH domain-binding protein 1	EHBP1	2,37346	2,5
Q8TBA6	Golgin subfamily A member 5	GOLGA5	3,0259	2,4
Q9BXF6	Rab11 family-interacting protein 5	RAB11FIP5	2,9101	2,4
Q7L804	Rab11 family-interacting protein 2	RAB11FIP2	3,33154	2,2
Q6IAA8	Ragulator complex protein LAMTOR1	LAMTOR1	3,23604	2,1
P61006	Ras-related protein Rab-8A	RAB8A	3,56486	2,1
P11717	Cation-independent mannose-6-phosphate receptor	IGF2R	5,71543	2,0
Q13190	Syntaxin-5	STX5	3,88884	2,0
Q15836;P63027	Vesicle-associated membrane protein 3;Vesicle-associated membrane protein 2	VAMP3;VAMP2	3,67019	2,0
Q92692	Nectin-2	PVRL2	3,06334	2,0
Q6NXT4	Zinc transporter 6	SLC30A6	3,47208	1,8
Q96A65	Exocyst complex component 4	EXOC4	2,51947	1,7
Q14141	Septin-6	Sept6	3,87782	1,7
Q04656	Copper-transporting ATPase 1	ATP7A	2,77415	1,7
Q7Z2W4	Zinc finger CCCH-type antiviral protein 1	ZC3HAV1	2,62567	1,6
P78310	Coxsackievirus and adenovirus receptor	CXADR	2,87956	1,4
P08195	4F2 cell-surface antigen heavy chain	SLC3A2	2,43497	1,4
P02786	Transferrin receptor protein 1;Transferrin receptor protein 1, serum form	TFRC	3,21618	1,3
Q07960	Rho GTPase-activating protein 1	ARHGAP1	2,65929	1,3
O60271	C-Jun-amino-terminal kinase-interacting protein 4	SPAG9	3,80826	1,3
P42167	Lamina-associated polypeptide 2, isoforms beta/gamma;Thymopoietin;Thymopentin	TMPO	3,54449	1,2
Q9BSJ8	Extended synaptotagmin-1	ESYT1	3,59064	1,0
Q14739	Lamin-B receptor	LBR	3,12029	0,8

Table 3: Enriched proteins in the RAB29-depended LRRK2 proximity proteome (FDR-controlled T-test).

1038 **Figures**

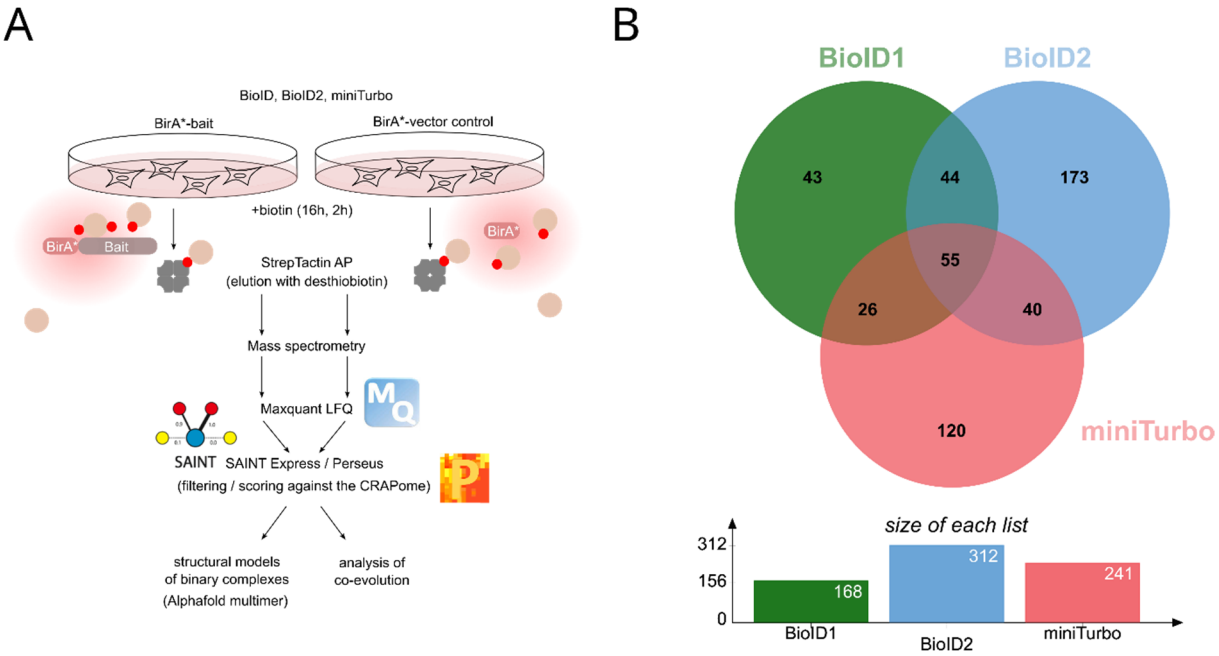

1039

1040 **Figure 1:** (A) Workflow of the BioID analysis and post processing of the data. (B) Overlap between the
1041 different BioID approaches. Enriched proteins were determined by relative label-free quantification
1042 (combined with an FDR-controlled T-test, p=0.05) of BioID LRRK2 vs the corresponding tag-only
1043 control: BioID1-LRRK2/BioID1: N=8, BioID2-LRRK2/BioID2: N=9, miniTurbo-LRRK2/miniTurbo: N=8.

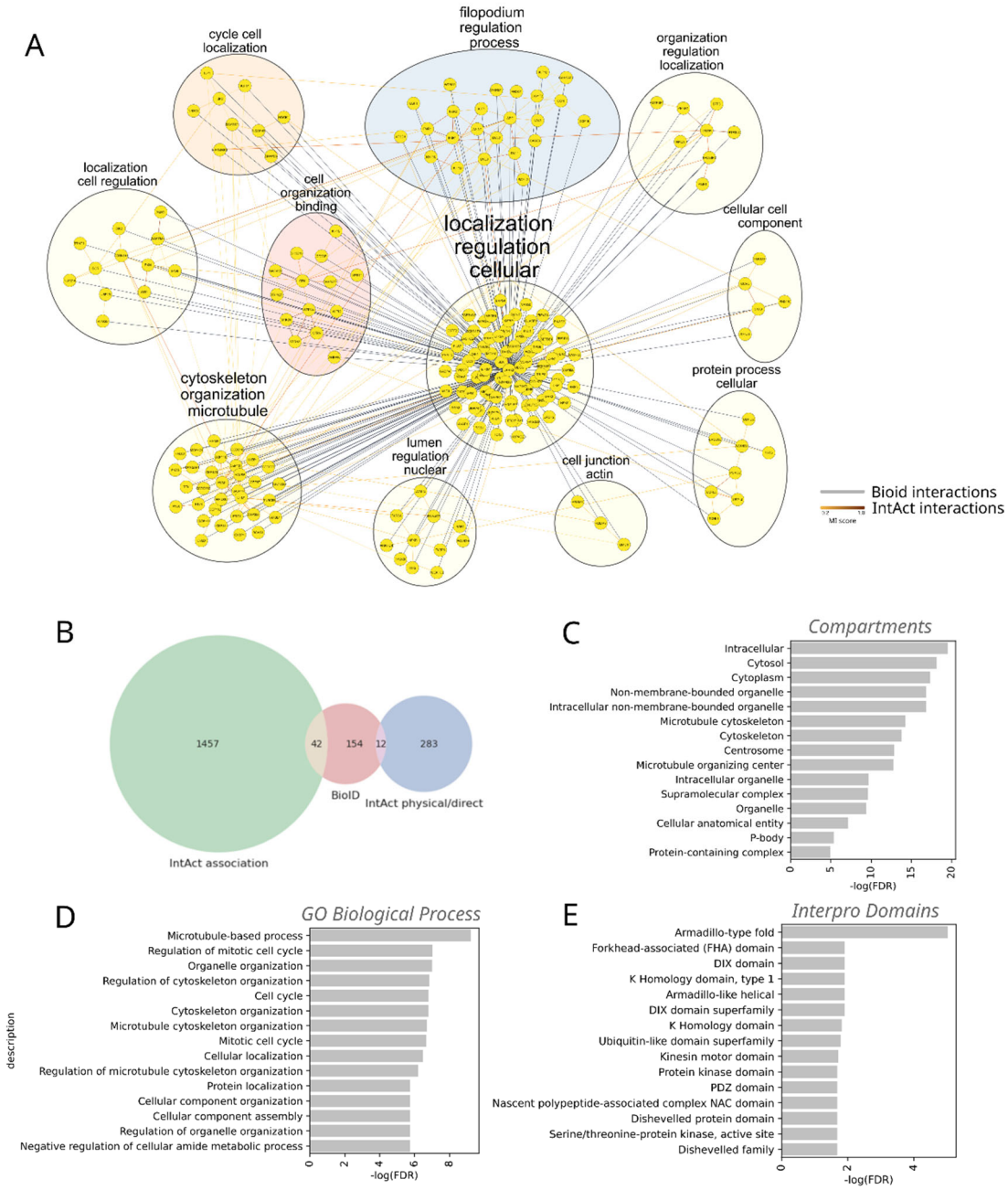

Figure 2: LRRK2 interactome functional enrichment. A) the LRRK2 BioID interaction network was mapped on known PPIs from IntAct via Cytoscape. The edges' color and thickness for mapped interactions are proportional to IntAct MI score, else they are colored in gray with constant thickness. Modules within the network have been identified through the Glay method of the Autoannotate app and nodes colored accordingly. Labels have been calculated using the 'Adjacent Words' of the WordCloud algorithm, considering the significantly enriched (FDR < 0.01) GO Biological processes and cellular compartments in which each given gene of the network participated; B) Venn diagram showing the overlap between the BioID interaction sets and known LRRK2 interactions in IntAct; barplots

1053 showing the top 15 **most** significant terms obtained through String's functional enrichment of C)
1054 Compartments, D) GO Biological Process and D) Interpro domains.

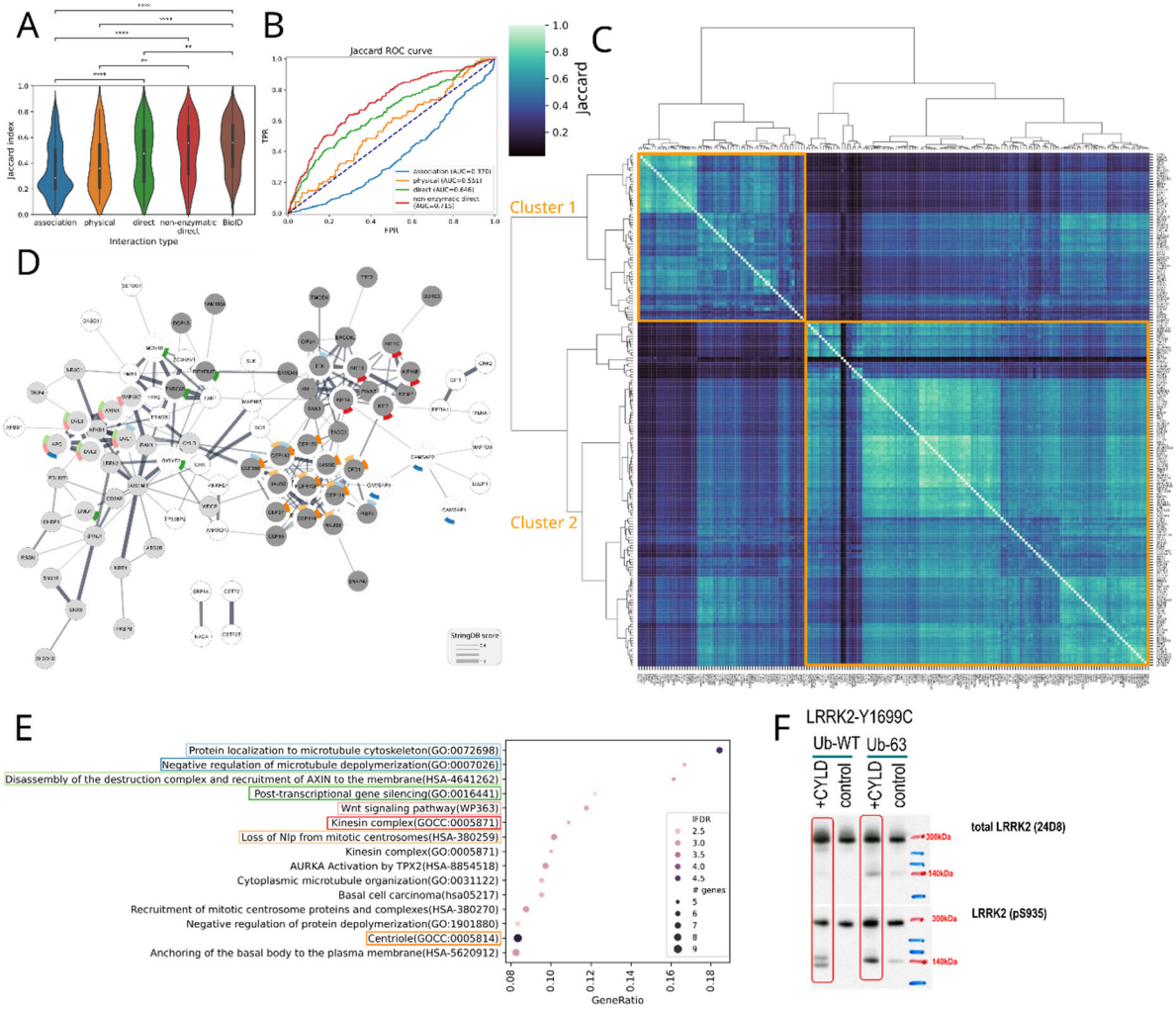

Figure 3: Co-evolution analysis of LRRK2 interactome. (A) Distribution of co-evolution metric (i.e. Jaccard score) among the different LRRK2 interaction sets, including IntAct interaction types and BIOID. P-values have been computed with the Wilcoxon rank-sum, two-sided test with Bonferroni correction (* $P < 0.05$, ** $P < 0.001$, *** $P < 0.001$, **** $P < 0.0001$). Violin plots show the median as the white central dot and first and third quartiles as bounds of the thicker black line (box); the whiskers extend to the last data point within 1.5 times the interquartile range (IQR) from the box's boundaries ; (B) predictiveness of LRRK2 **interaction type** via co-evolution (C) Heatmap showing the hierarchical clustering based on the degree of co-evolution (Jaccard score) of the LRRK2 proximity proteome; (D) String network of the proteins most co-evolved with LRRK2 participating to cluster 2. Nodes are colored in gray or light-gray according to modules membership determined with the MCL approach available from the Cytoscape clusterMaker app. Node rims are colored according to enriched processes; (E) Dot plot showing top 15 significantly enriched (FDR < 0.01) categories from the string network of cluster 2. Values on the x axis display the ratio of genes of the term participating to the network over the total number of genes in that category. The ratio of the dot is proportional to the number of genes of that category in the network, while the node color is the

1071 darker the more significant is the category enrichment. Only categories with at least 5 genes have been
1072 displayed. Representative, enriched categories have been colored with the same color scheme as in
1073 panel (D); (F) Effect of CYLD co-expression on LRRK2 stability in HEK293T. Cells were transfected with
1074 LRRK2 Y1699C and either with WT-ubiquitin (WT-Ub) or Ubiquitin-K63 (Ub-63) which can only be
1075 Ubiquitin-conjugated at lysine 63. In addition, CYLD or a vector control (pcDNA3.0) were co-expressed.

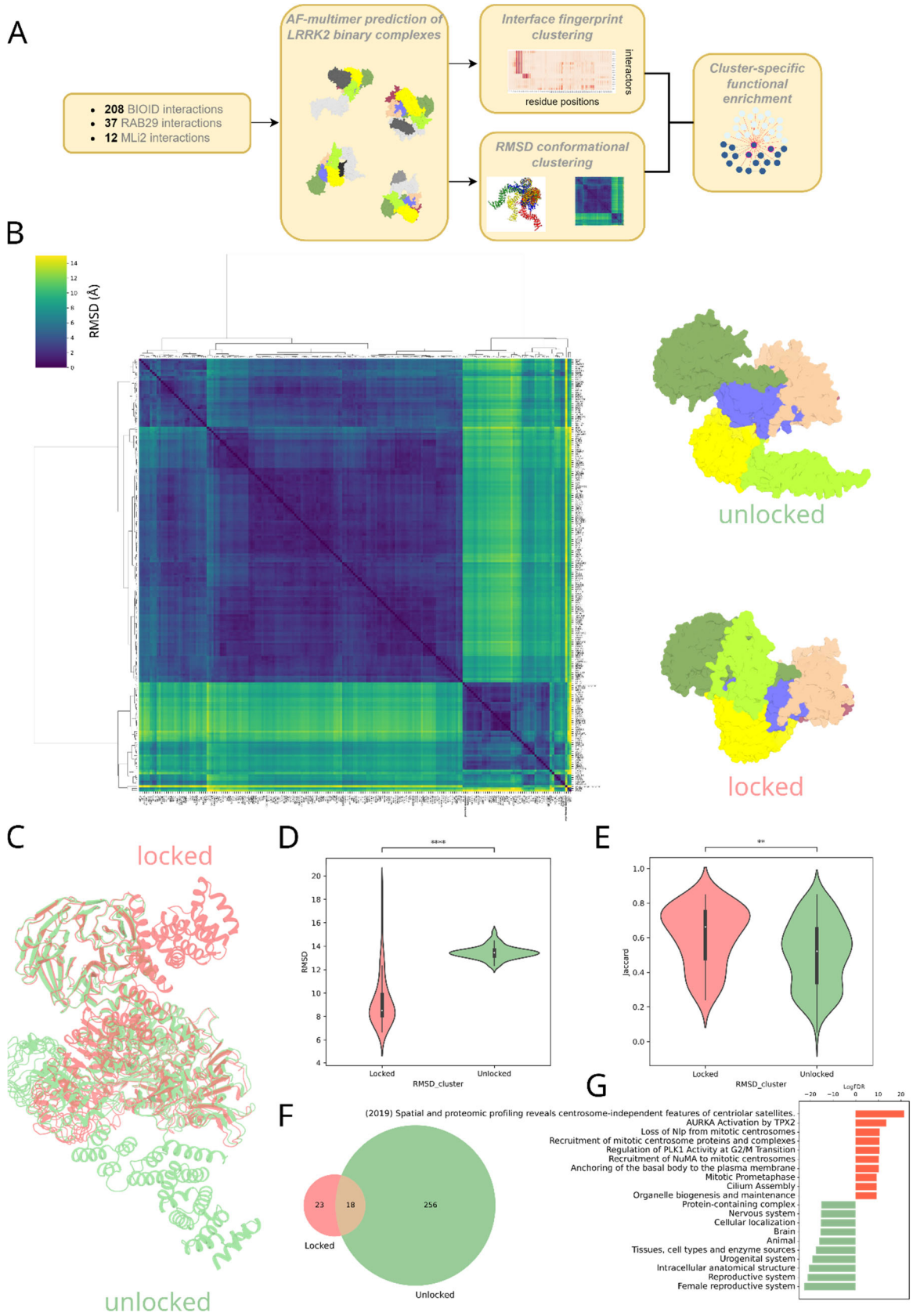

Figure 4: 3D complexes prediction and analysis of LRRK2 interactome (A) workflow of the structural bioinformatics analysis of LRRK2 interactome; (B) on the left the heatmap showing the hierarchical clustering based on pairwise RMSD calculation of LRRK2's chain in the different complexes. On the right two representative conformations of LRRK2 in the "locked" and "unlocked" conformation to mark

1081 the two main clusters; (C) cartoon representation of “locked” (tomato) and “unlocked” (light green)
1082 superimposed LRRK2 conformations; (D) violin plot of the distribution of RMSD calculated with respect
1083 to the reference LRRK2 experimental structure (PDB 7LHW) for the locked and unlocked clusters. Color
1084 scheme as in (C); (E) distribution of the Jaccard score for the locked and unlocked clusters. Color
1085 scheme as in (C). P-values for violin plots in D and E have been computed with the Wicoxon
1086 rank-sum, two-sided test (* $P < 0.05$, ** $P < 0.001$, *** $P < 0.001$, **** $P < 0.0001$). Violin plots
1087 show the median as the white central dot and first and third quartiles as bounds of the thicker
1088 black line (box); the whiskers extend to the last data point within 1.5 times the interquartile
1089 range (IQR) from the box’s boundaries; (F) Venn diagram of the enriched terms in the locked and
1090 unlocked clusters. Color scheme as in (C); (E) Top 10 exclusively enriched (FDR<0.01) terms in the
1091 locked and unlocked clusters.

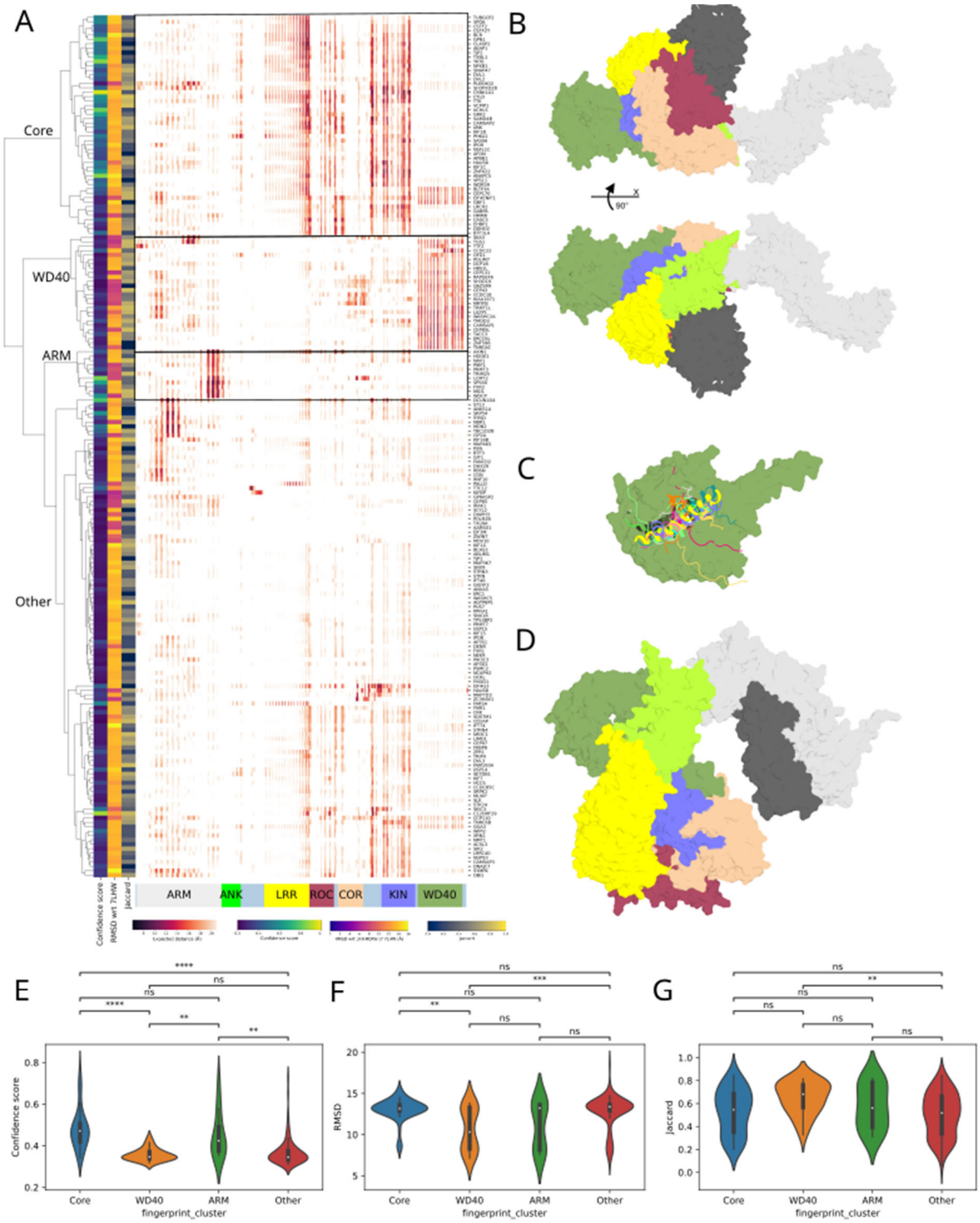

Figure 5: Interface analysis of LRRK2's 3D interactome (A) interface fingerprint of the LRRK2 complexes via distogram calculation. Cells contain the minimum expected distance obtained from the distograms of any residue of each interactor (row) to every residue in LRRK2 (column). Rows are color annotated based on confidence score, Jaccard and RMSD from reference LRRK2 structure (PDB: 7LHW); (B) representative structure of the Core cluster (i.e. LRRK2-ANAPC5 complex); (C) representative structures of the WD40 cluster; (D) representative structures of the ARM binding mode cluster (i.e.

1099 LRRK2- DCUN1D4 complex); distribution among different interface cluster of the (E) confidence score,
1100 (F) RMSD and (G) Jaccard score descriptors. P-values have been computed with the Wicoxon rank-
1101 sum, two-sided test with Bonferroni correction (* $P < 0.05$, ** $P < 0.001$, *** $P < 0.001$, ****
1102 $P < 0.0001$). Violin plots show the median as the white central dot and first and third quartiles
1103 as bounds of the thicker black line (box); the whiskers extend to the last data point within 1.5
1104 times the interquartile range (IQR) from the box's boundaries.

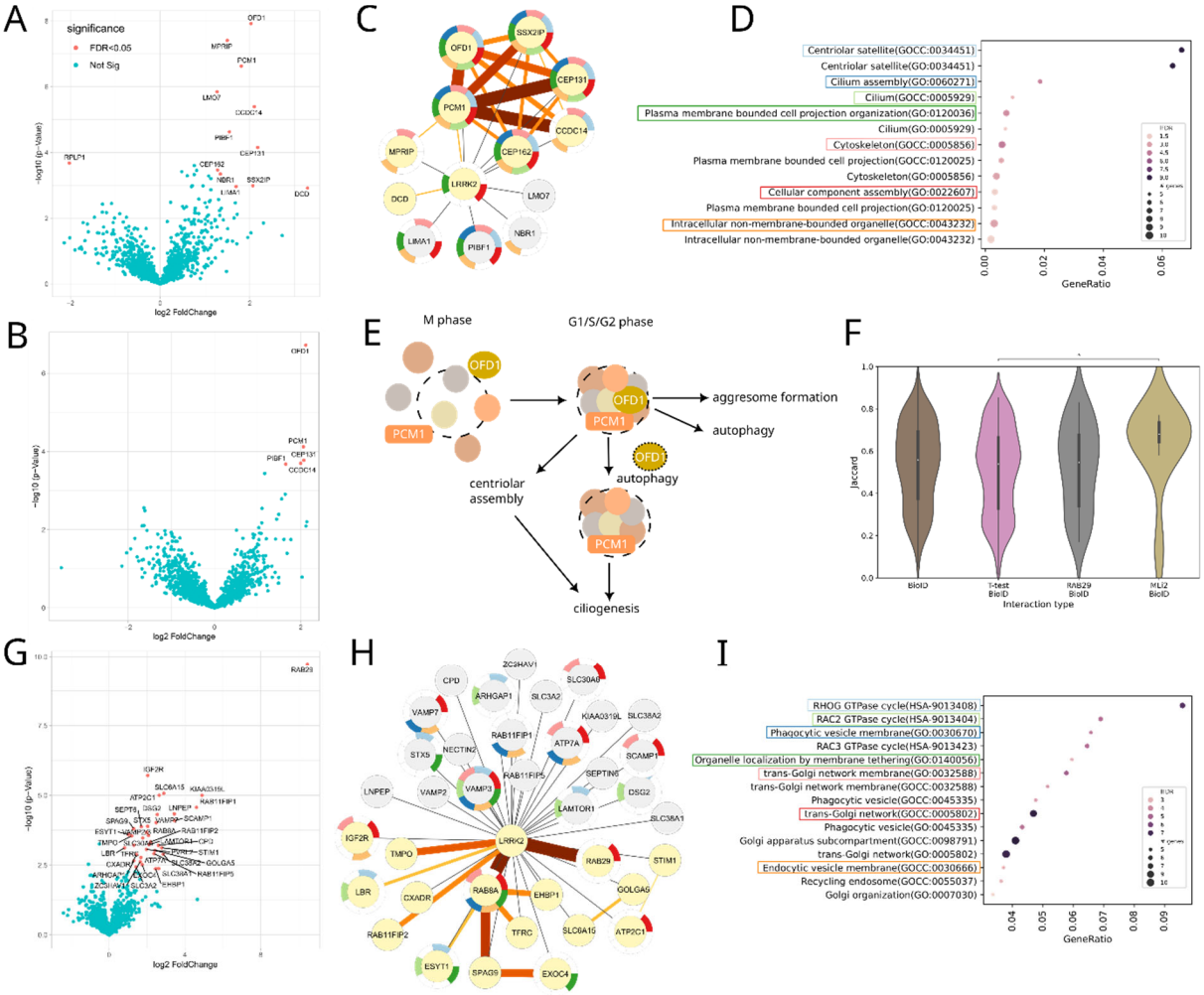

Figure 6: Different effects of type I and type II inhibitors and RAB29 on the LRRK2 proximity proteome. (A) MLi-2 vs DMSO. (B) MLi-2 vs GZD-824; (C) Stringified network of the MLi-2 interactome from (A) mapped to IntAct known interactions. Edges' color and thickness for mapped interactions are proportional to IntAct MI score, else they are colored in gray with constant thickness. Node rims are colored according to enriched processes; (D) Dot plot showing top 15 significantly enriched (FDR < 0.01) categories from the LRRK2-MLi-2 interactome. Values on the x axis display the ratio of genes of the term participating to the network over the total number of genes in that category. The ratio of the dot is proportional to the number of genes of that category in the network, while the node color is the darker the more significant is the category enrichment. Only categories with at least 5 genes have been displayed. Representative, enriched categories have been colored with the same color scheme as in panel C. (E) Scheme highlighting the function of centriolar satellites and the core protein PCM1 in ciliation ((Hori and Toda, 2017), modified) (F) Violin plot reporting the Jaccard Score distribution in different data sets. P-values have been computed with the Wicoxon rank-sum, two-sided test with Bonferroni correction (* $P < 0.05$). Violin plots show the median as the white central dot and first and third quartiles as bounds of the thicker black line (box); the whiskers extend to

1121 the last data point within 1.5 times the interquartile range (IQR) from the box's boundaries;
1122 (G) mt-LRRK2 proximity proteome in dependence of RAB29 co-expression: RAB29 redirects LRRK2 to
1123 lysosomal PPI networks; (H) Stringified network of the RAB29 over-expression interactome from (G)
1124 mapped to IntAct known interactions. Edges' color and thickness for mapped interactions are
1125 proportional to IntAct MI score, else they are colored in gray with constant thickness. Node rims are
1126 colored according to enriched processes; (I) Dot plot showing top 15 significantly enriched (FDR < 0.01)
1127 categories from the LRRK2-RAB29 over-expression interactome. Values on the x axis display the ratio
1128 of genes of the term participating to the network over the total number of genes in that category. The
1129 ratio of the dot is proportional to the number of genes of that category in the network, while the node
1130 color is the darker the more significant is the category enrichment. Only categories with at least 5
1131 genes have been displayed. Representative, enriched categories have been colored with the same
1132 color scheme as in panel H.

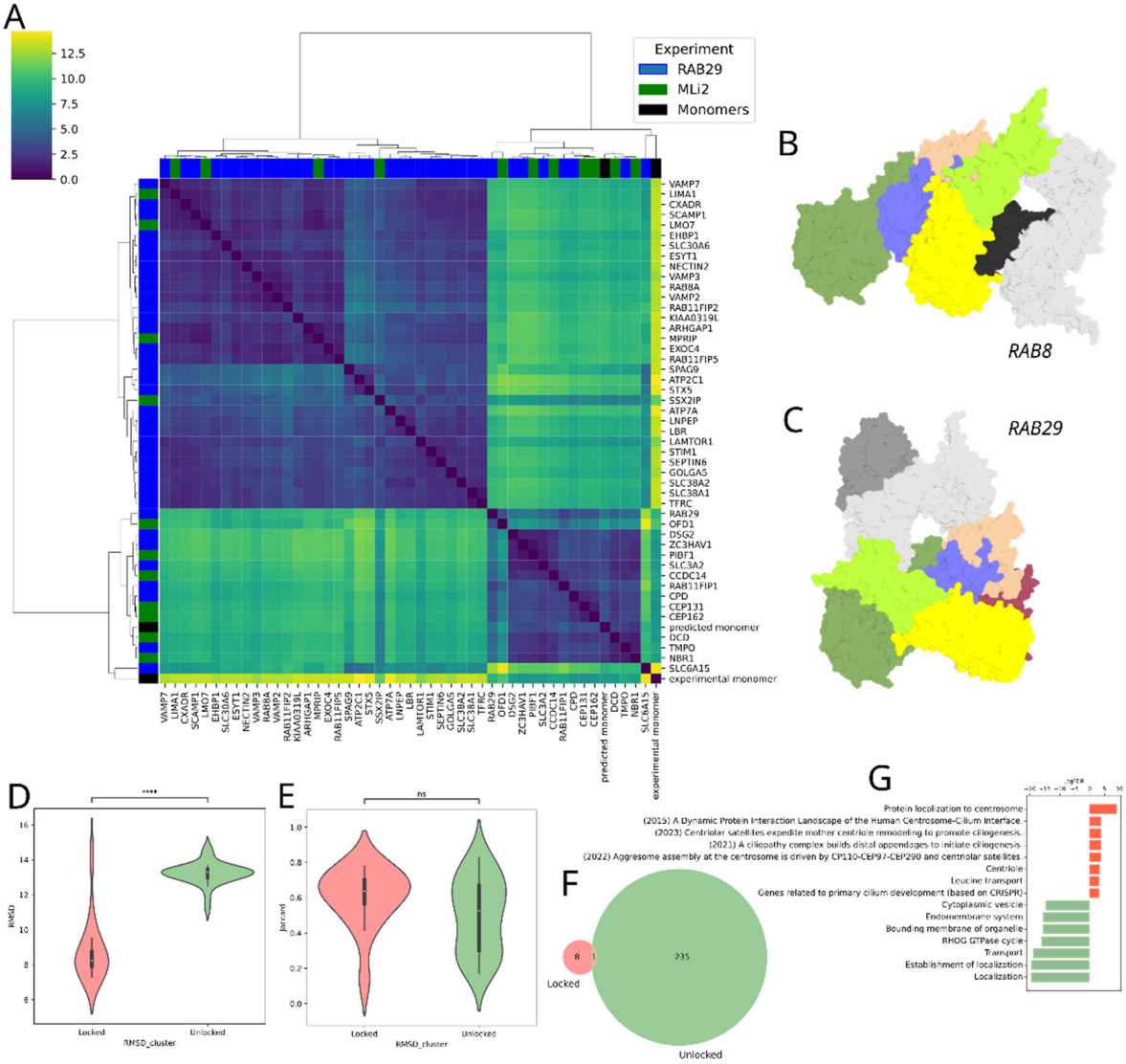

Figure 7: AF-structural modeling of MLi-2 and Rab29 interactomes. (A) Hierarchical clustering of pairwise RMSD of LRRK2 chain in the different complexes; B) LRRK2-RAB8A predicted complex; (C) LRRK2-RAB29 predicted complex; (D) violin plot of the distribution of RMSD calculated with respect to the reference LRRK2 experimental structure (PDB 7LHW) for the locked and unlocked clusters. Color scheme as in 4C; (E) distribution of the Jaccard score for the locked and unlocked clusters. Color scheme as in 4C. P-values in violin plots in (D) and (E) have been computed with the Wicoxon rank-sum, two-sided test (* $P < 0.05$, ** $P < 0.001$, *** $P < 0.001$, **** $P < 0.0001$). Violin plots show the median as the white central dot and first and third quartiles as bounds of the thicker black line (box); the whiskers extend to the last data point within 1.5 times the interquartile range (IQR) from the box's boundaries; (F) Venn diagram of the enriched terms in the locked and

1144 unlocked clusters. Color scheme as in 4C; (G) Top exclusively enriched (FDR<0.01) terms in the locked
1145 and unlocked clusters. Color scheme as in 4C.

1146 **Supplemental Information**

1147 Supplemental tables (2 separate files):

1148 **Supplemental Table 1:** LRRK2 proximity proteomes obtained with BioID1, BioID2 and miniTurbo as
1149 well as the Rab29-dependent LRRK2-mT and the inhibitor-dependent LRRK2-mT proximity proteomes.

1150 **Supplemental Table 2:** co-evolutionary and structural features of BioID interactors

1151 **Supplemental Table 3**: over-representation analysis of protein clusters defined via co-evolution

1152 **Supplemental Table 4:** over-representation analysis of protein clusters defined via RMSD clustering of
1153 AF-multimer predicted complexes

1154 **Supplemental Table 5:** over-representation analysis of protein clusters defined via Interaction
1155 fingerprint clustering of AF-multimer predicted complexes

1156 **Supplemental Table 6**: over-representation analysis of protein clusters defined via RMSD clustering of
1157 AF-multimer predicted complexes of the RAB29-overexpression and MLi-2 interactomes

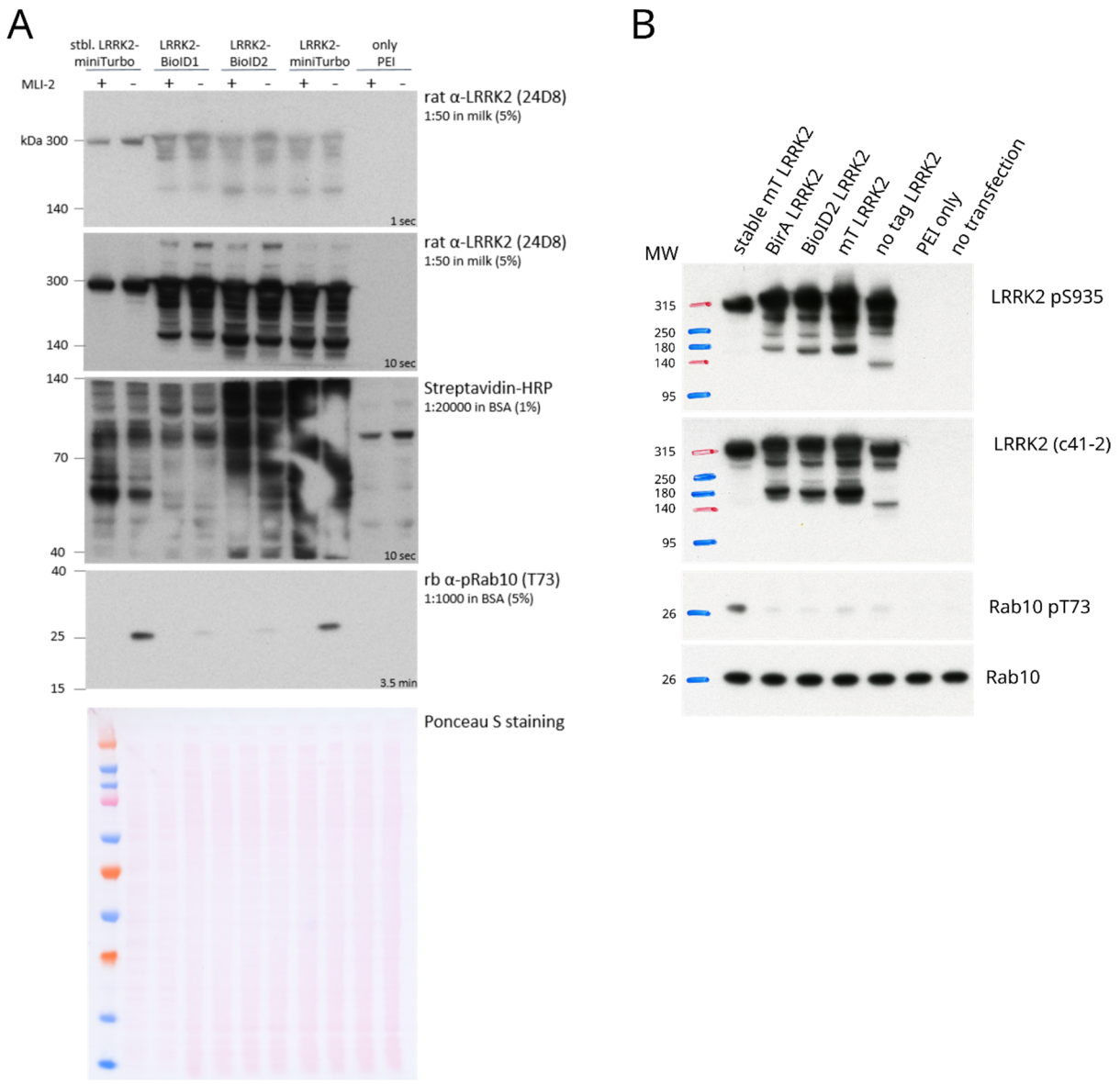

Supplemental Figure 1: Western blot, pRab10, pS935 and biotinylation – comparison BioID1, BioID2, miniTurbo. To ensure functional BioID-fusion proteins, LRRK2 phosphorylation at S935 and Rab10 phosphorylation was assessed. (A) The different BioID LRRK2 constructs show sufficient biotinylation of proteins as well as MLi-2-responsive Rab10 phosphorylation. (B) All constructs are phosphorylated at S935 (top panel). Replication of LRRK2-mediated Rab10 phosphorylation (last panel) demonstrating functional BioID fusion proteins.

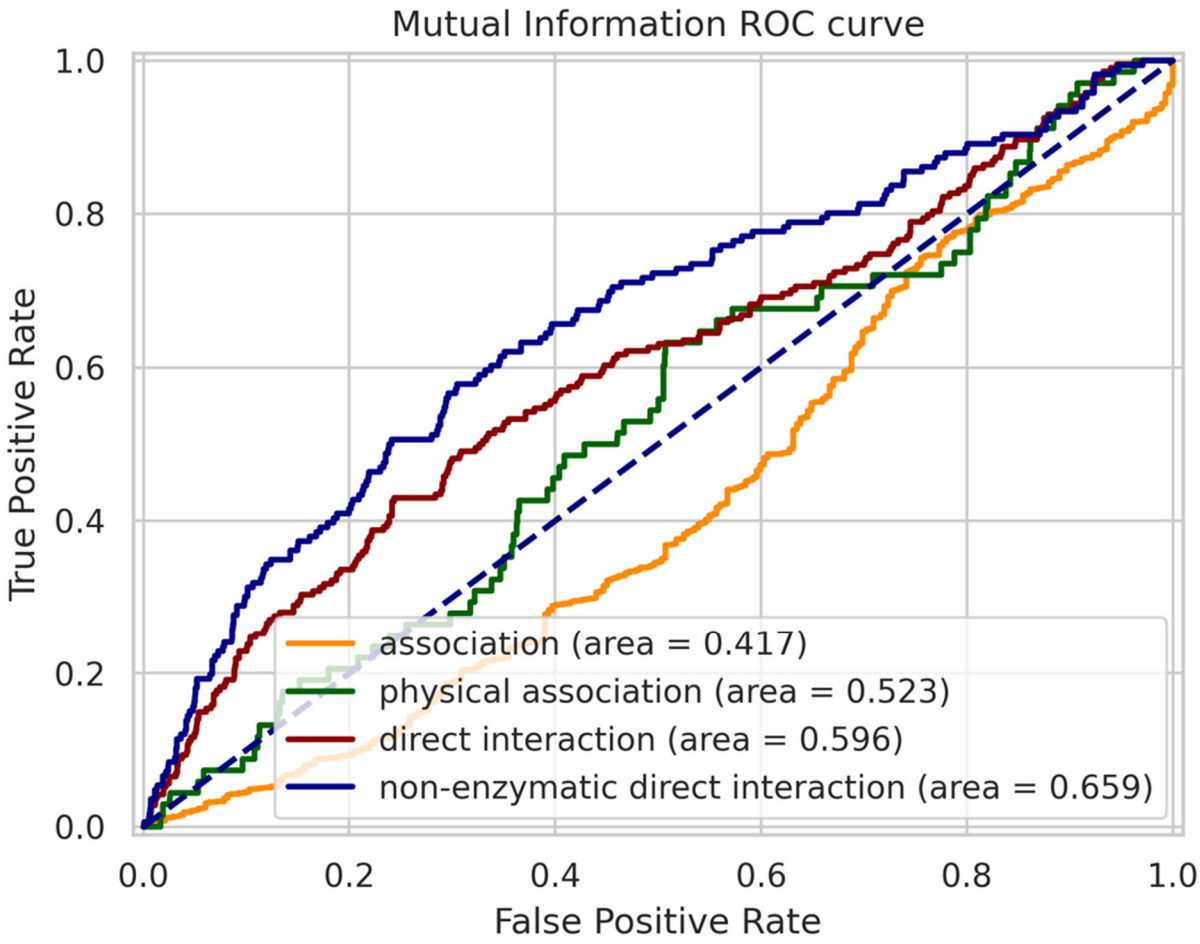

Supplemental Figure 2: ROC Curve of prediction with Mutual Information (MI) of LRRK2's IntAct interaction types.

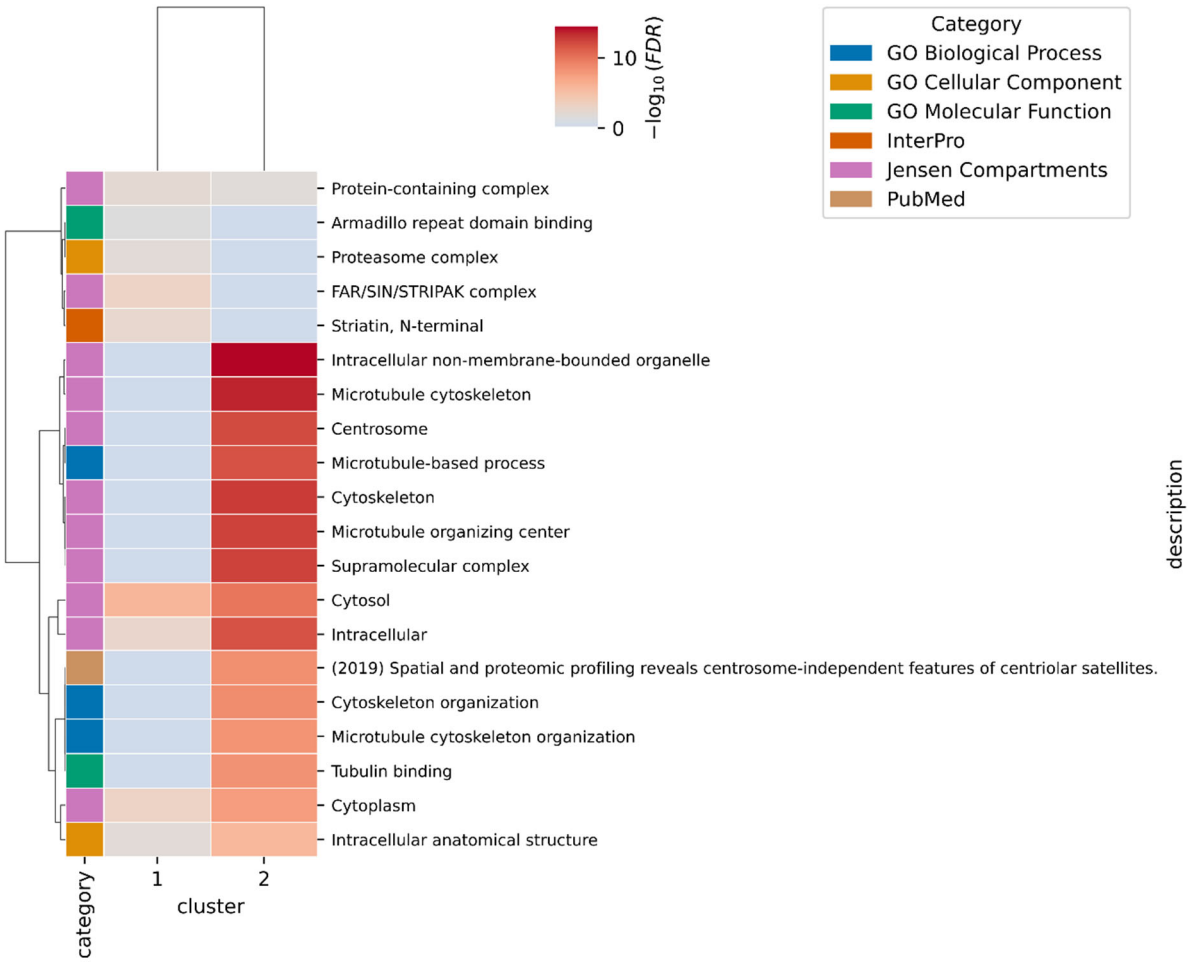

Supplemental Figure 3: heatmap with cluster specific, significantly enriched processes (FDR < 0.01; StringDB) obtained from coevolution (Jaccard)-based clustering of the LRRK2 BioID interactome.

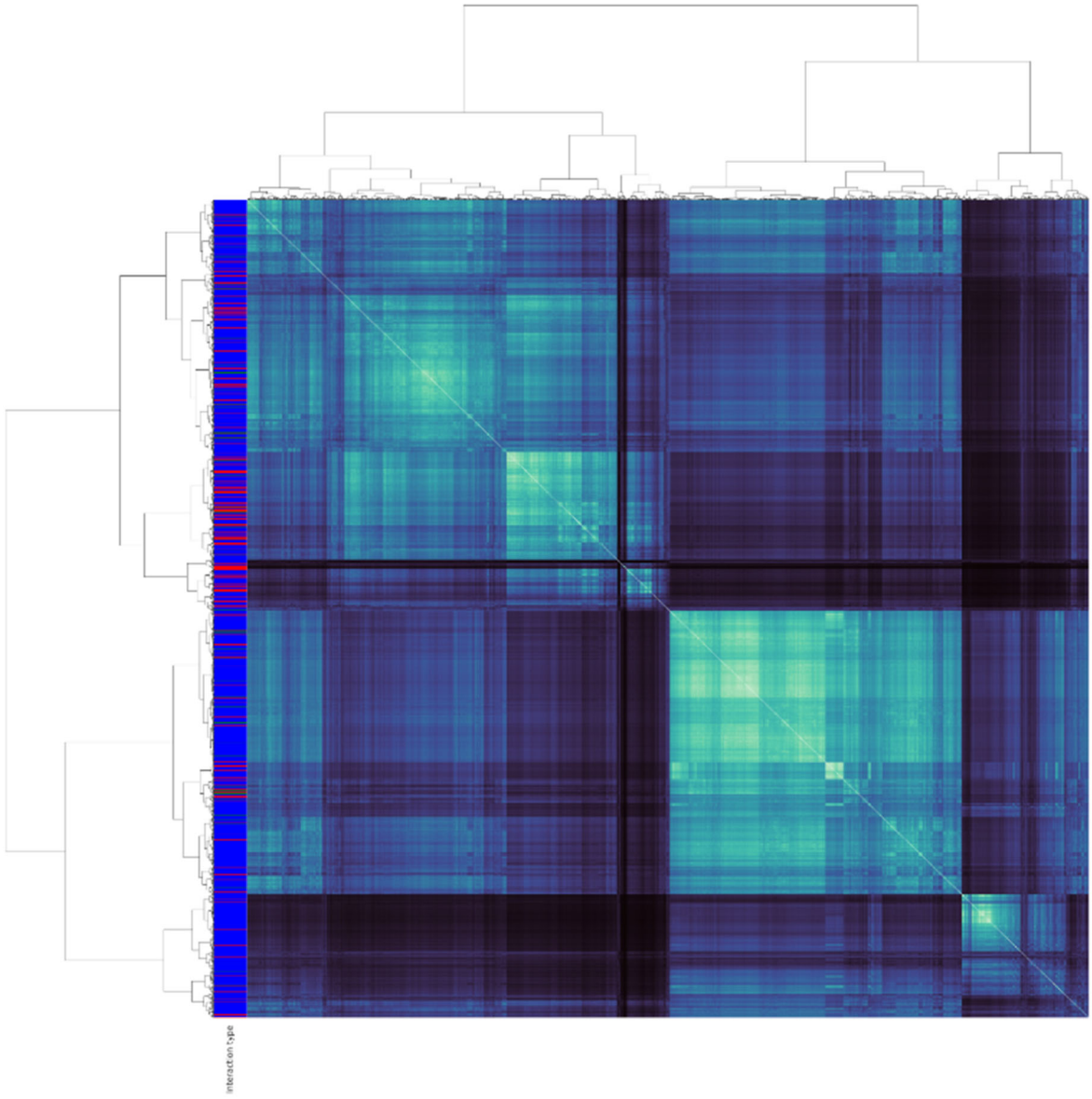

Supplemental Figure 4: heatmap displaying the coevolution (Jaccard)-based hierarchical clustering of the LRRK2's IntAct interactome. Colored bars provide IntAct's interaction type annotation.

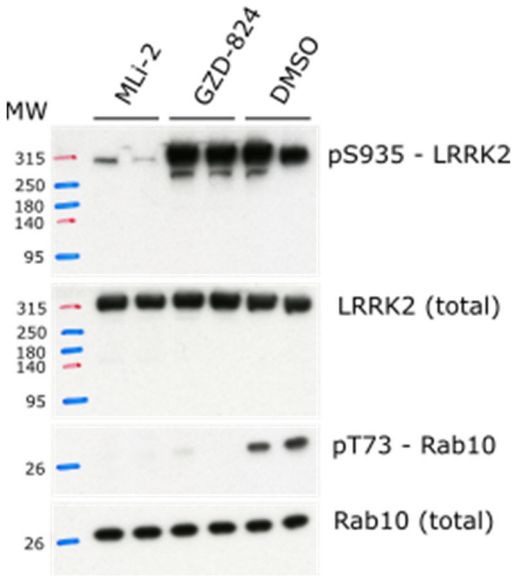

Supplemental Figure 5: Western blot demonstrating sufficient LRRK2 inhibition for MLi-2 and GZD-824 in a HEK293 line stably expressing miniTurbo LRRK2. Both inhibitors show a sufficient inhibition of Rab10 phosphorylation at 1µM. While the type I inhibitor shows the characteristic loss of LRRK2 pS935 phosphorylation, the type II inhibitor GZD-824 does not alter pS935 phosphorylation (Tasegian et al., 2021).

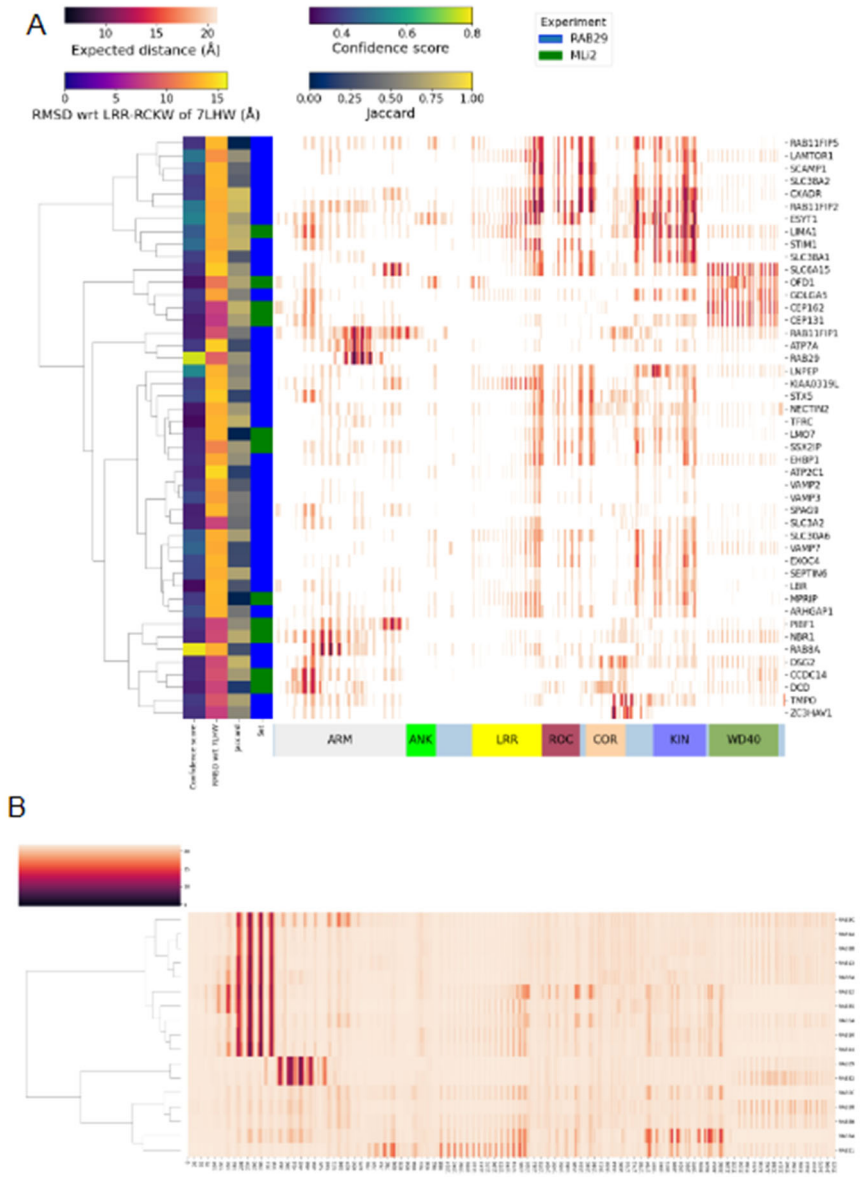

Supplemental Figure 6: (A) interaction fingerprint clustering of LRRK2's modulators (MLi-2 and RAB29) interactomes. Cells contain the minimum expected distance obtained from the distograms of any residue of each interactor (row) to every residue in LRRK2 (column). Rows are color annotated based on confidence score, Jaccard, RMSD from reference LRRK2 structure (PDB: 7LHW) and experiment type (either MLi-2 or RAB29 over-expression); (B) interaction fingerprint of LRRK2 and interacting RABs (from IntAct).